Reciprocal representation of encoded features by cortical excitatory and inhibitory neuronal populations.

Authors

A.J. DUSZKIEWICZ[1,2], S. SKROMNE CARRASCO [1], P. ORHAN[1], E. BROWN[1], E. OWCZAREK[1], G. R. VITE[1], E. R. WOOD[2], A. PEYRACHE[1,*]

1Montreal Neurological Institute and Hospital, McGill University, Montreal, QC, Canada
[2]Centre for Discovery Brain Sciences, University of Edinburgh, Edinburgh, UK

Abstract

In the cortex, the interplay between excitation and inhibition determines the fidelity of neuronal representations. However, while the receptive fields of excitatory neurons are often fine-tuned to the encoded features, the principles governing the tuning of inhibitory neurons are still elusive. We addressed this problem by recording populations of neurons in the postsubiculum (PoSub), a cortical area where the receptive fields of most excitatory neurons correspond to a specific head-direction (HD). In contrast to PoSub-HD cells, the tuning of fast-spiking (FS) cells, the largest class of cortical inhibitory neurons, was broad and heterogeneous. However, we found that PoSub-FS cell tuning curves were fine-tuned in the spatial frequency domain, resulting in various radial symmetries in their HD tuning. In addition, the average frequency spectrum of PoSub-FS cell populations was virtually indistinguishable from that of PoSub-HD cells but different from that of the upstream thalamic HD cells, suggesting that this co-tuning in the frequency domain has a local origin. Two observations corroborated this hypothesis. First, PoSub-FS cell tuning was independent of upstream thalamic inputs. Second, PoSub-FS cell tuning was tightly coupled to PoSub-HD cell activity even during sleep. Together, these findings provide evidence that the resolution of neuronal tuning is an intrinsic property of local cortical networks, shared by both excitatory and inhibitory cell populations. We hypothesize that this reciprocal encoding supports two parallel streams of information processing in thalamocortical networks.

Main

Understanding the nature of neural computation is traditionally addressed by determining how external and internal signals are represented at the neuronal level [1–5]. While neurons in many sensory and other cortical systems encode high-dimensional features [6–9], their tuning can only be measured for a limited range of the possible feature space – that is, the variables measured in the experiments [10]. In comparison, the feature space of the HD system is relatively simple, with excitatory neurons firing for specific direction of the head in the horizontal plane [4,11–13]. The HD signal is transmitted from the anterodorsal nucleus (ADN) of the thalamus to cortical recipient neurons in the PoSub [4,11–15]. Importantly, this simplicity allows for a full characterization of neuronal tuning during natural behaviors [16,17].

Cortical inhibition plays a critical role in shaping the tuning of neuronal responses [18–27]. Yet, the tuning of inhibitory neurons, especially FS cells, is often considered to be broad [28–34] or irregular [35–41]. By interrogating the HD tuning of PoSub-FS neurons in relation to tuning of local excitatory cell and upstream thalamic inputs, we show that PoSub-FS neurons represent, on the population level, features with equal resolution when compared to their local but not upstream excitatory counterparts.

High-density recordings in the PoSub of freely moving mice.

We first established the functional border between PoSub and posterior retrosplenial cortex using a Neuropixel linear electrode array (**Figure 1A-B**). The step-like increase in average HD tuning along this axis was then used to guide the pre-implanted, microdrive-mounted 64-channel linear electrode arrays and record single-unit activity in PoSub. Probes were implanted either vertically (n = 931 units from 14 mice, range: 46-101 units per recording, **Figure S1A-C**) or parallel to PoSub cell layers (n = 1999 units from 18 mice, range: 42-185 units per recording, **Figure 1C-D**, **Figure S1E**) and electrode positions were later confirmed histologically (**Figure S1D**). As we found no differences in cell properties across the two datasets (data not shown), they were pooled for further analysis. All recording sessions consisted of square open field exploration and sleep epochs, with a subset of sessions extended to include a triangular open field or a cue rotation task (**Table S1**). PoSub units were subdivided into putative excitatory (PoSub-EX) cells (n = 1835) and putative PoSub-FS cells (n = 427) based on mean firing rate and waveform shape (**Figure S1F**). A subset of PoSub-EX cells whose HD information exceeded the 99th percentile of the time-reversed control distribution (see **Methods**) were classified as PoSub-HD cells (> 0.2 bits/spike, n = 1602, 87% of PoSub-EX cells; **Figure S1F**).

PoSub-FS cells share functional properties with canonical HD cells

At the population level, we observed that the quantity of HD information conveyed by PoSub-FS cells was significantly higher than that of the time-reversed control population (**Figure 1E**). However, in contrast to canonical HD cells, individual PoSub-FS cells had complex, often multipeaked tuning curves not confined to discrete HD values. We hypothesized that since PoSub-

FS cells receive inputs from local PoSub-HD cells (**Figure S1G**), they would share their functional properties. Indeed, the tuning of PoSub-FS cells was stable within a single exploration epoch (**Figure 1F)** and independent of the enclosure geometry (**Figure 1G**), reflecting the properties of canonical PoSub-HD cells (**Figure S1H**). Importantly, in a cue rotation paradigm (**Figure 1H, Figure S1I**) PoSub-FS cell tuning followed the rotated distal landmark in concert with PoSub-HD cells (**Figure 1I-J**). Thus, while PoSub-FS cells, in contrast to canonical HD cells, exhibit irregular HD tuning curves, they are functionally integrated into the cortical HD system.

HD tuning of PoSub-HD and PoSub-FS cells is equivalent in the Fourier space

We next aimed to establish whether the tuning of PoSub-FS cells was related to the tuning of local HD cells. To address this question, we compared the HD tuning of PoSub-FS cells with that of PoSub-HD cells as well as with that of the HD cells in the upstream ADN (ADN-HD cells; n = 97 cells from 8 mice; **Figure 2A-B, Figure S2A**). In mice, ADN-HD neurons tend to have broader HD tuning curves than PoSub-HD neurons (**Figure 2C, Figure S2B-D**), a property independent of their tendency to fire in anticipation of future HD [42] (**Figure S2C-D**). We thus utilized these differences in tuning curve shape between the two populations to establish their relative influence on the tuning of PoSub-FS cells. Importantly, HD tuning of PoSub-FS cells cannot be directly compared with that of canonical HD cells due to their irregular, often multipeaked shape. In order to overcome this, we transformed the HD tuning curves from the spatial domain ("HD space") to the spatial frequency domain ("Fourier space"). (**Figure 2D**; see **Methods**). Each tuning curve was thus represented as a sum of sine waves ("Fourier components") whose frequencies are equal to the harmonics of the unit circle, corresponding to periods from 360° (fundamental frequency) to 2° (highest possible harmonic, equal to twice the tuning curve sampling bin). In turn, each Fourier component could be described in terms of its amplitude (or "power") and phase, which reflects the relative orientation of that component. Each tuning curve was thus associated with an individual "Fourier signature", consisting of relative powers of its Fourier components. Across the cell population, the Fourier power decayed rapidly as a function of frequency. Hence, for clarity, we focused our analysis on the relative power of the first ten Fourier components which contained, on average, 98% of the total power.

Canonical HD cells, sharply tuned in HD space, showed broad and stereotyped tuning in Fourier space, with power distributed across several Fourier components and each successive component showing progressively less power. We found that Fourier signatures of PoSub-HD and ADN-HD cells often differed between the two regions (**Figure 2D**, top): ADN-HD Fourier signatures tended to be skewed towards lower components compared to PoSub-HD cells, reflecting their broader tuning curves. We confirmed this relationship between Fourier signature and tuning curve width by performing the Fourier decomposition of simulated HD tuning curves of different width (**Figure 2E**).

In contrast, PoSub-FS cells exhibited highly heterogenous Fourier signatures, with many cells broadly tuned in HD space but narrowly tuned in the Fourier space, i.e. showing high power for only one Fourier component (**Figure 2D**, bottom). We hypothesized that while Fourier signatures

of individual PoSub-FS cells reflect their heterogenous tuning shapes, overall they are ought to be constrained by the tuning properties of their main HD inputs. Indeed, we found that the average Fourier signature of PoSub-FS cells was similar to the Fourier signature of PoSub-HD cells but unlike that of ADN-HD cells (**Figure 2F-G**, **Figure S2F**). Like hippocampal place cells, HD cells can sometimes have multiple receptive fields [38] which could affect the average Fourier signature of an HD cell population. However, the reported differences were even more pronounced when the dataset was limited to HD cells with a single receptive field (**Figure S2G-K**). Thus, although HD tuning curves of individual PoSub-HD and PoSub-FS cells appear strikingly different, on a population level they share the same underlying Fourier power spectrum.

Yet, the HD and FS cell populations differed in two main aspects. First, while the shape of the Fourier signature was largely uniform across HD cells, it was highly variable across PoSub-FS cells (**Figure 2H**), reflecting narrow tuning of PoSub-FS cells in the Fourier space (**Figure 2D**). Hence, the Fourier spectrum of the local HD signal is distributed among the PoSub-FS cell population rather than being homogeneously reflected within each individual cell. Second, in individual HD cells, the phases of the different Fourier components were correlated with each other, as expected for any symmetrical function with a single maximum (**Figure 2I,** *left* and *middle*). In contrast, the Fourier components of individual PoSub-FS cells had random phases relative to each other (**Figure 2I**, *right*), explaining the apparent irregularity of their HD tuning.

To gain further insights into the shape of PoSub-FS cell tuning curves independently of their relative orientation, we computed an auto-correlation function for each cell by correlating its tuning curve with itself at different circular shifts. We then projected the resulting auto-correlograms onto a 2-dimensional space using the Isomap dimensionality reduction algorithm [43] (**Figure 2J**). The resulting projection reflects the heterogeneity of PoSub-FS cell tuning curve shape across the population (compared to control data, **Figure S2M**). Importantly, the triangular shape of this unsupervised embedding revealed that a large portion of the power was concentrated in the first three Fourier components. PoSub-FS cells located at each vertex of the triangle showed pure 1-, 2-, or 3-fold symmetrical HD tuning (**Figure 2K, Figure S2L)**, reflecting their narrow tuning in the Fourier space. Still, this distribution was a continuum and other PoSub-FS cells were characterized by a subset of Fourier components (**Figure S2N**). We then projected the data again into the same 2-dimensional space, this time adding the auto-correlograms of PoSub-HD and ADN-HD cells. We found that PoSub-HD and ADN-HD cell auto-correlograms occupy compact subspaces within the broader distribution, reflecting their relative homogeneity (**Figure 2L**). The auto-correlogram distribution of PoSub-HD cells occupied the centre of PoSub-FS cell distribution while that of ADN-HD cells was closer to the periphery (**Figure 2M**), confirming the observations of differences in average Fourier signatures (**Figure 2F-G**). In conclusion, the shapes of PoSub-FS cell tuning curves were broadly distributed and each was unique. Yet, their tuning resolution was shared with PoSub-HD cells, but not ADN-HD cells.

PoSub-FS cells receive directionally uniform input from the anterior thalamus

Thalamocortical neurons exert a strong excitatory drive onto cortical FS cells [44,45], including in the ADN-PoSub circuit [46]. To determine whether upstream thalamic inputs shape PoSub-FS cell tuning, we selectively manipulated the strength (or "gain") of the thalamic input from ADN to PoSub and quantified the effect of this manipulation on the tuning of PoSub-FS cells. We reasoned that if each PoSub-FS cell receives non-uniform thalamic HD input, increasing input gain should result in non-uniform (multiplicative) modulation of their HD tuning. In contrast, if the thalamic input is uniform, PoSub-FS cell tuning should be uniformly (additively) modulated [47].

The ADN is strongly innervated by inhibitory afferents from the thalamic reticular nucleus (TRN, **Figure 3A**; **Figure S3A-B**) [48,49]. We leveraged this specific inhibitory pathway to selectively increase the activity of ADN-HD cells. To that end, we injected a Cre-dependent AAV-ArchT into TRN of VGAT-Cre mice and recorded ensembles of anterior thalamic neurons (**Figure 3B**; n = 127 thalamic cells, including 52 HD cells, from 3 mice). Targeted illumination of ADN (thus inactivating the inhibitory presynaptic terminals of the TRN neurons) resulted in a net increase in the firing rate of ADN-HD cells but not that of not directionally-tuned neurons (non-HD cells) recorded during the same sessions (**Figure 3C**), further confirming preferential TRN innervation of ADN over other anterior thalamic nuclei (**Figure S3A**). Contrary to long-term disinhibition [49], short-term disinhibition of ADN-HD cells was not associated with broadening of their tuning curves (**Figure 3D, Figure S3D**), This manipulation therefore selectively increased the gain of the thalamic HD signal without affecting its resolution. We thus used this method to characterize the effects of thalamic gain modulation on the HD tuning of PoSub neurons. We recorded ensembles of PoSub neurons in VGAT-Cre mice injected with AAV-ArchT (n = 83 PoSub-HD cells, 47 PoSub-FS cells from 5 mice) or a control viral vector (n = 89 PoSub-HD cells, 38 PoSub-FS cells from 3 mice; **Figure 3E**) bilaterally into TRN. Similarly to the upstream ADN-HD cells, PoSub-HD and PoSub-FS cells increased their firing rates (**Figure 3F-G, Figure S3C**) without significantly distorting their HD tuning (**Figure 3H, Figure S3E**).

We then computed, for each cell, linear regression between HD tuning curves in the baseline condition and under high thalamic gain (i.e. ADN disinhibition). The slope of the linear fit denotes the multiplicative modulation of tuning by thalamic gain, while the intercept denotes additive modulation [47] (**Figure 3I-J**). Thus, a slope above 1 indicates the presence of multiplicative gain and a positive intercept indicates the presence of additive gain. When computing the tuning curves, we used larger angular bins (6°) instead of smoothing in order to ensure that individual points on the tuning curve are independent from one another. We then assessed the contribution of these additive and multiplicative factors to the tuning modulation of PoSub-HD and PoSub-FS cells. On a population level, the modulation of PoSub-HD cells was purely multiplicative (**Figure 3K-M**), indicating that they receive HD-specific thalamic inputs. Indeed, this high degree of multiplicative modulation largely reflected the modulation of the upstream ADN-HD cells (**Figure S3F-H**). In contrast, the modulation of PoSub-FS cell tuning was exclusively additive (**Figure 3L-N**), indicating that they receive uniform thalamic input for all directions.

PoSub-FS cell tuning arises from coupling to the HD ring attractor

Finally, in order to exclude the possibility that the tuning of PoSub-FS cells is determined by external factors like vision, we sought to establish whether their activity is coupled to the internal attractor dynamics of the in absence of sensory input. The HD signal in the ADN-PoSub pathway is coherently organized into a 1-dimentional (1-D) ring attractor even during sleep when sensory inputs are virtually absent [14,50]. We thus tested whether the tuning of PoSub-FS cells relies on the intrinsic dynamics of the HD cell attractor network during sleep. To address this question, we analyzed ensemble activity during Rapid Eye Movement (REM) sleep, when the coordination of PoSub-HD cells is virtually indistinguishable from wakefulness (**Figure S4A-B**).

We first sought to establish whether the temporal coupling between individual PoSub-FS and PoSub-HD cells was preserved during REM sleep. In order to account for the coupling to the population firing rate irrespective of any specific tuning [51]**,** we quantified the pairwise coupling between PoSub cells using a General Linear Model (GLM). While both PoSub-HD and PoSub-FS cells showed strong coupling to the population (**Figure S4C**), we found that the polarity of the GLM cross-coupling coefficient ('beta') between PoSub-HD cell pairs was preserved across wakefulness (WAKE) and Rapid Eye Movement (REM) sleep (**Figure 4A-C**, top). For example, PoSub-HD cell pairs co-active during wakefulness showed a high degree of co-activity during REM sleep, while those that were negatively coupled during WAKE were also negatively coupled during REM. Similarly, PoSub-FS cell pairs also preserved their coupling to across WAKE and REM, albeit to a smaller degree than PoSub-HD cell pairs (**Figure 4A-C**, middle). Importantly, the two cell populations were also coupled to each other across WAKE and REM (**Figure 4A-C**, bottom). Predictably, for all cell pairs beta polarity depended on the HD tuning relationship within each cell pair during both WAKE and REM (**Figure S4D**). Overall, these results indicate that the activity of PoSub-FS cells is coupled to the internal attractor dynamics of the HD system.

While stable correlation structures among cell pairs constitute strong evidence for coupling of PoSub-FS cells to the HD attractor network, large-scale population recordings enable a more direct visualization and analysis of the 1-D ring attractor manifold that constrains the activity of individual HD cells. We thus asked whether the activity of PoSub-FS cells is constrained by the same ring attractor manifold as that of PoSub-HD cells. To that end, we applied Isomap [43] to HD cell population vectors in order to visualize the 1-D ring manifold of PoSub-HD cell population activity during WAKE [50,52] (**Figure 4D, Figure S4E-G**). We first confirmed that the internal representation of the animal's current HD during WAKE can be decoded in an unsupervised manner from the manifold as the angular coordinate ('virtual HD') of each HD cell population vector on the ring. The HD tuning curves of both PoSub-HD and PoSub-FS cells computed using virtual HD values during WAKE were equivalent to those computed using real HD values (**Figure 4E, Figure S4J**). During REM sleep the HD system disengages from the outside world while at the same time representing an internally-generated, drifting virtual HD [14,50]. We thus applied Isomap to REM PoSub-HD population vectors and computed the corresponding virtual HD (**Figure 4F, Figure S4H-I**). As expected, HD tuning curves of PoSub-HD cells generated internally from the animal's virtual HD during REM were similar to their WAKE counterparts (**Figure S4K**). Importantly, HD tuning of PoSub-FS cells could also be recovered during REM

based solely on the virtual HD obtained from the HD ring attractor manifold (**Figure 4G).** Taken together, these results indicate that the activity of PoSub-FS cells is restricted by the topology of the HD cell attractor and is largely independent of external inputs.

Discussion

In summary, our results establish that PoSub-FS cells, despite having irregular HD tuning curves, share many tuning properties with canonical HD cells: their tuning is stable over time and across environments and is anchored to distal landmarks. However, unlike their canonical counterparts, FS cells represent HD in a reciprocal encoding space – the Fourier domain. When this is taken into account, the tuning curves of inhibitory and excitatory cell populations in the PoSub share the same tuning resolution. Finally, we found that this relationship is a local property of the network as the tuning of PoSub-FS cells does not depend on the upstream thalamic input from the ADN and is tightly coupled to the intrinsic dynamics of PoSub-HD cells. We predict that this functional relationship between excitatory and inhibitory cell populations is a general feature of cortical neuronal systems.

FS cells integrate and reflect the activity of anatomically proximal excitatory neurons [28,31,40,53]. This raises the possibility that PoSub-HD neurons are organized in local assemblies representing spatial symmetries. Previous studies have reported symmetries in HD tuning in the retrosplenial cortex [54] and in spatial tuning in the medial entorhinal cortex in the form of grid cells [3], border [55] and band cells [56], as well as neurons modulated by environment boundaries [57] and axis of travel [58] in the subiculum. The retrosplenial cortex, medial entorhinal cortex, and subiculum are three of the main output structures of the PoSub. While HD cell activity in the ADN-PoSub network is crucial for grid cell activity in the medial entorhinal cortex [59], it remains to be shown whether the organization of PoSub-HD cells into functional and symmetrical assemblies influences downstream spatial symmetries.

Finally, thalamocortical circuits have inspired the architecture of deep neural nets in machine learning, whereby units in each layer perform a convolution over finite patches of the previous layer to achieve a representation of increasing complexity [60,61]. Here, we have shown that inhibitory neurons likely receive homogeneous inputs from thalamic neurons, irrespective of their preferred direction. This raises the intriguing possibility that inhibitory neurons can learn a representation from the entire input layer, and not only from a subset of units corresponding to a local region in feature space. As FS cells are fine-tuned in Fourier space, feedforward thalamocortical inhibition [44,45] may thus be akin to a projection of the entire input layer activity onto a Fourier basis determined by the intrinsic tuning properties of the cortical area.

References

1. Hubel, D. H. & Wiesel, T. N. Receptive fields, binocular interaction and functional architecture in the cat's visual cortex. *J. Physiol.* **160**, 106–154 (1962).
2. O'Keefe, J. & Dostrovsky, J. The hippocampus as a spatial map. Preliminary evidence from unit activity in the freely-moving rat. *Brain Res.* **34**, 171–175 (1971).
3. Hafting, T., Fyhn, M., Molden, S., Moser, M.-B. & Moser, E. I. Microstructure of a spatial map in the entorhinal cortex. *Nature* **436**, 801–806 (2005).
4. Taube, J. S., Muller, R. U. & Ranck, J. B. Head-direction cells recorded from the postsubiculum in freely moving rats. I. Description and quantitative analysis. *J. Neurosci.* **10**, 420–435 (1990).
5. Harris, K. D. Neural signatures of cell assembly organization. *Nat. Rev. Neurosci.* **6**, 399–407 (2005).
6. Stringer, C., Pachitariu, M., Steinmetz, N., Carandini, M. & Harris, K. D. High-dimensional geometry of population responses in visual cortex. *Nature* **571**, 361–365 (2019).
7. Barlow, H. B. Possible principles underlying the transmission of sensory messages. *Sens. Commun.* 217–234 (1961).
8. Simoncelli, E. P. & Olshausen, B. A. Natural Image Statistics and Neural Representation. *Annu. Rev. Neurosci.* **24**, 1193–1216 (2001).
9. Rigotti, M. *et al.* The importance of mixed selectivity in complex cognitive tasks. *Nature* **497**, 585–590 (2013).
10. Gao, P. *et al.* A theory of multineuronal dimensionality, dynamics and measurement. 214262 (2017) doi:10.1101/214262.
11. Taube, J. S. Head direction cells recorded in the anterior thalamic nuclei of freely moving rats. *J. Neurosci.* **15**, 70–86 (1995).
12. Taube, J. S. The head direction signal: origins and sensory-motor integration. *Annu. Rev. Neurosci.* **30**, 181–207 (2007).
13. Sharp, P. E., Blair, H. T. & Cho, J. The anatomical and computational basis of the rat head-direction cell signal. *Trends Neurosci.* **24**, 289–294 (2001).
14. Peyrache, A., Lacroix, M. M., Petersen, P. C. & Buzsáki, G. Internally organized mechanisms of the head direction sense. *Nat. Neurosci.* **18**, 569–575 (2015).
15. Peyrache, A., Duszkiewicz, A. J., Viejo, G. & Angeles-Duran, S. Thalamocortical processing of the head-direction sense. *Prog. Neurobiol.* **183**, 101693 (2019).
16. Peyrache, A., Schieferstein, N. & Buzsáki, G. Transformation of the head-direction signal into a spatial code. *Nat. Commun.* **8**, 1752 (2017).
17. Ajabi, Z., Keinath, A. T., Wei, X.-X. & Brandon, M. P. Population dynamics of the thalamic head direction system during drift and reorientation. *bioRxiv* (2021).
18. Isaacson, J. S. & Scanziani, M. How Inhibition Shapes Cortical Activity. *Neuron* **72**, 231–243 (2011).
19. Borg-Graham, L. J., Monier, C. & Fregnac, Y. Visual input evokes transient and strong shunting inhibition in visual cortical neurons. *Nature* **393**, 369–372 (1998).
20. Wehr, M. & Zador, A. M. Balanced inhibition underlies tuning and sharpens spike timing in auditory cortex. *Nature* **426**, 442–446 (2003).
21. Sillito, A. M. Inhibitory processes underlying the directional specificity of simple, complex and hypercomplex cells in the cat's visual cortex. *J. Physiol.* **271**, 699–720 (1977).
22. Wilson, N. R., Runyan, C. A., Wang, F. L. & Sur, M. Division and subtraction by distinct cortical inhibitory networks *in vivo*. *Nature* **488**, 343–348 (2012).
23. Lee, S.-H. *et al.* Activation of specific interneurons improves V1 feature selectivity and visual perception. *Nature* **488**, 379–383 (2012).
24. Royer, S. *et al.* Control of timing, rate and bursts of hippocampal place cells by dendritic and somatic inhibition. *Nat. Neurosci.* **15**, 769–775 (2012).

25. Pi, H.-J. *et al.* Cortical interneurons that specialize in disinhibitory control. *Nature* **503**, 521–524 (2013).
26. Simonnet, J. *et al.* Activity dependent feedback inhibition may maintain head direction signals in mouse presubiculum. *Nat. Commun.* **8**, 16032 (2017).
27. Ozeki, H., Finn, I. M., Schaffer, E. S., Miller, K. D. & Ferster, D. Inhibitory Stabilization of the Cortical Network Underlies Visual Surround Suppression. *Neuron* **62**, 578–592 (2009).
28. Kerlin, A. M., Andermann, M. L., Berezovskii, V. K. & Reid, R. C. Broadly Tuned Response Properties of Diverse Inhibitory Neuron Subtypes in Mouse Visual Cortex. *Neuron* **67**, 858–871 (2010).
29. Sohya, K., Kameyama, K., Yanagawa, Y., Obata, K. & Tsumoto, T. GABAergic Neurons Are Less Selective to Stimulus Orientation than Excitatory Neurons in Layer II/III of Visual Cortex, as Revealed by In Vivo Functional Ca2+ Imaging in Transgenic Mice. *J. Neurosci.* **27**, 2145–2149 (2007).
30. Niell, C. M. & Stryker, M. P. Highly Selective Receptive Fields in Mouse Visual Cortex. *J. Neurosci.* **28**, 7520–7536 (2008).
31. Hofer, S. B. *et al.* Differential connectivity and response dynamics of excitatory and inhibitory neurons in visual cortex. *Nat Neurosci* **14**, 1045–1052 (2011).
32. Hirsch, J. A. *et al.* Functionally distinct inhibitory neurons at the first stage of visual cortical processing. *Nat. Neurosci.* **6**, 1300–1308 (2003).
33. Cardin, J. A., Palmer, L. A. & Contreras, D. Stimulus Feature Selectivity in Excitatory and Inhibitory Neurons in Primary Visual Cortex. *J. Neurosci.* **27**, 10333–10344 (2007).
34. Nowak, L. G., Sanchez-Vives, M. V. & McCormick, D. A. Lack of Orientation and Direction Selectivity in a Subgroup of Fast-Spiking Inhibitory Interneurons: Cellular and Synaptic Mechanisms and Comparison with Other Electrophysiological Cell Types. *Cereb. Cortex* **18**, 1058–1078 (2008).
35. Wilson, M. A. & McNaughton, B. L. Dynamics of the hippocampal ensemble code for space. *Science* **261**, 1055–1058 (1993).
36. Maurer, A. P., Cowen, S. L., Burke, S. N., Barnes, C. A. & McNaughton, B. L. Phase Precession in Hippocampal Interneurons Showing Strong Functional Coupling to Individual Pyramidal Cells. *J. Neurosci.* **26**, 13485–13492 (2006).
37. Buetfering, C., Allen, K. & Monyer, H. Parvalbumin interneurons provide grid cell-driven recurrent inhibition in the medial entorhinal cortex. *Nat. Neurosci.* **17**, 710–718 (2014).
38. Tukker, J. J., Tang, Q., Burgalossi, A. & Brecht, M. Head-Directional Tuning and Theta Modulation of Anatomically Identified Neurons in the Presubiculum. *J. Neurosci.* **35**, 15391–15395 (2015).
39. Ego-Stengel, V. & Wilson, M. A. Spatial selectivity and theta phase precession in CA1 interneurons. *Hippocampus* **17**, 161–174 (2007).
40. Geisler, C., Robbe, D., Zugaro, M., Sirota, A. & Buzsáki, G. Hippocampal place cell assemblies are speed-controlled oscillators. *Proc. Natl. Acad. Sci.* **104**, 8149 (2007).
41. Peng, Y. *et al.* Spatially structured inhibition defined by polarized parvalbumin interneuron axons promotes head direction tuning. *Sci. Adv.* **7**, eabg4693.
42. Blair, H. T. & Sharp, P. E. Anticipatory head direction signals in anterior thalamus: evidence for a thalamocortical circuit that integrates angular head motion to compute head direction. *J. Neurosci.* **15**, 6260 (1995).
43. Tenenbaum, J. B., Silva, V. de & Langford, J. C. A Global Geometric Framework for Nonlinear Dimensionality Reduction. *Science* **290**, 2319–2323 (2000).
44. Cruikshank, S. J., Lewis, T. J. & Connors, B. W. Synaptic basis for intense thalamocortical activation of feedforward inhibitory cells in neocortex. *Nat. Neurosci.* **10**, 462–468 (2007).
45. Gabernet, L., Jadhav, S. P., Feldman, D. E., Carandini, M. & Scanziani, M. Somatosensory Integration Controlled by Dynamic Thalamocortical Feed-Forward Inhibition. *Neuron* **48**, 315–327 (2005).
46. Nassar, M. *et al.* Anterior Thalamic Excitation and Feedforward Inhibition of Presubicular Neurons Projecting to Medial Entorhinal Cortex. *J. Neurosci.* **38**, 6411–6425 (2018).

47. Arandia-Romero, I., Tanabe, S., Drugowitsch, J., Kohn, A. & Moreno-Bote, R. Multiplicative and Additive Modulation of Neuronal Tuning with Population Activity Affects Encoded Information. *Neuron* **89**, 1305–1316 (2016).
48. Gonzalo-Ruiz, A. & Lieberman, A. R. Topographic organization of projections from the thalamic reticular nucleus to the anterior thalamic nuclei in the rat. *Brain Res. Bull.* **37**, 17–35 (1995).
49. Vantomme, G. *et al.* A Thalamic Reticular Circuit for Head Direction Cell Tuning and Spatial Navigation. *Cell Rep.* **31**, 107747 (2020).
50. Chaudhuri, R., Gercek, B., Pandey, B., Peyrache, A. & Fiete, I. The intrinsic attractor manifold and population dynamics of a canonical cognitive circuit across waking and sleep. *Nat. Neurosci.* **22**, 1512–1520 (2019).
51. Gardner, R. J., Lu, L., Wernle, T., Moser, M.-B. & Moser, E. I. Correlation structure of grid cells is preserved during sleep. *Nat. Neurosci.* **22**, 598 (2019).
52. Viejo, G. & Peyrache, A. Precise coupling of the thalamic head-direction system to hippocampal ripples. *Nat. Commun.* **11**, 2524 (2020).
53. Bock, D. D. *et al.* Network anatomy and in vivo physiology of visual cortical neurons. *Nature* **471**, 177–182 (2011).
54. Jacob, P.-Y. *et al.* An independent, landmark-dominated head-direction signal in dysgranular retrosplenial cortex. *Nat. Neurosci.* **20**, 173–175 (2017).
55. Solstad, T., Boccara, C. N., Kropff, E., Moser, M.-B. & Moser, E. I. Representation of Geometric Borders in the Entorhinal Cortex. *Science* **322**, 1865–1868 (2008).
56. Krupic, J., Burgess, N. & O'Keefe, J. Neural representations of location composed of spatially periodic bands. *Science* **337**, 853–857 (2012).
57. Lever, C., Burton, S., Jeewajee, A., O'Keefe, J. & Burgess, N. Boundary Vector Cells in the Subiculum of the Hippocampal Formation. *J. Neurosci.* **29**, 9771–9777 (2009).
58. Olson, J. M., Tongprasearth, K. & Nitz, D. A. Subiculum neurons map the current axis of travel. *Nat. Neurosci.* **20**, 170–172 (2017).
59. Winter, S. S., Clark, B. J. & Taube, J. S. Disruption of the head direction cell network impairs the parahippocampal grid cell signal. *Science* **347**, 870–874 (2015).
60. LeCun, Y., Bengio, Y. & Hinton, G. Deep learning. *Nature* **521**, 436–444 (2015).
61. Richards, B. A. *et al.* A deep learning framework for neuroscience. *Nat. Neurosci.* **22**, 1761–1770 (2019).
62. Pachitariu, M., Steinmetz, N., Kadir, S., Carandini, M. & Harris, K. D. Kilosort: realtime spike-sorting for extracellular electrophysiology with hundreds of channels. *bioRxiv* 061481 (2016) doi:10.1101/061481.
63. Hazan, L., Zugaro, M. & Buzsáki, G. Klusters, NeuroScope, NDManager: A free software suite for neurophysiological data processing and visualization. *J. Neurosci. Methods* **155**, 207–216 (2006).
64. Rossant, C. *et al.* Spike sorting for large, dense electrode arrays. *Nat. Neurosci.* **19**, 634–641 (2016).
65. Skaggs, W. E., McNaughton, B. L., Gothard, K. M. & Markus, E. J. An information-theoretic approach to deciphering the hippocampal code. in *Proceedings of the 5th International Conference on Neural Information Processing Systems* 1030–1037 (Morgan Kaufmann Publishers Inc., 1992).
66. Johnson, A., Seeland, K. & Redish, A. D. Reconstruction of the postsubiculum head direction signal from neural ensembles. *Hippocampus* **15**, 86–96 (2005).
67. Watson, B. O., Levenstein, D., Greene, J. P., Gelinas, J. N. & Buzsáki, G. Network Homeostasis and State Dynamics of Neocortical Sleep. *Neuron* **90**, 839–852 (2016).
68. Levenstein, D., Buzsáki, G. & Rinzel, J. NREM sleep in the rodent neocortex and hippocampus reflects excitable dynamics. *Nat. Commun.* **10**, 2478 (2019).

Figures

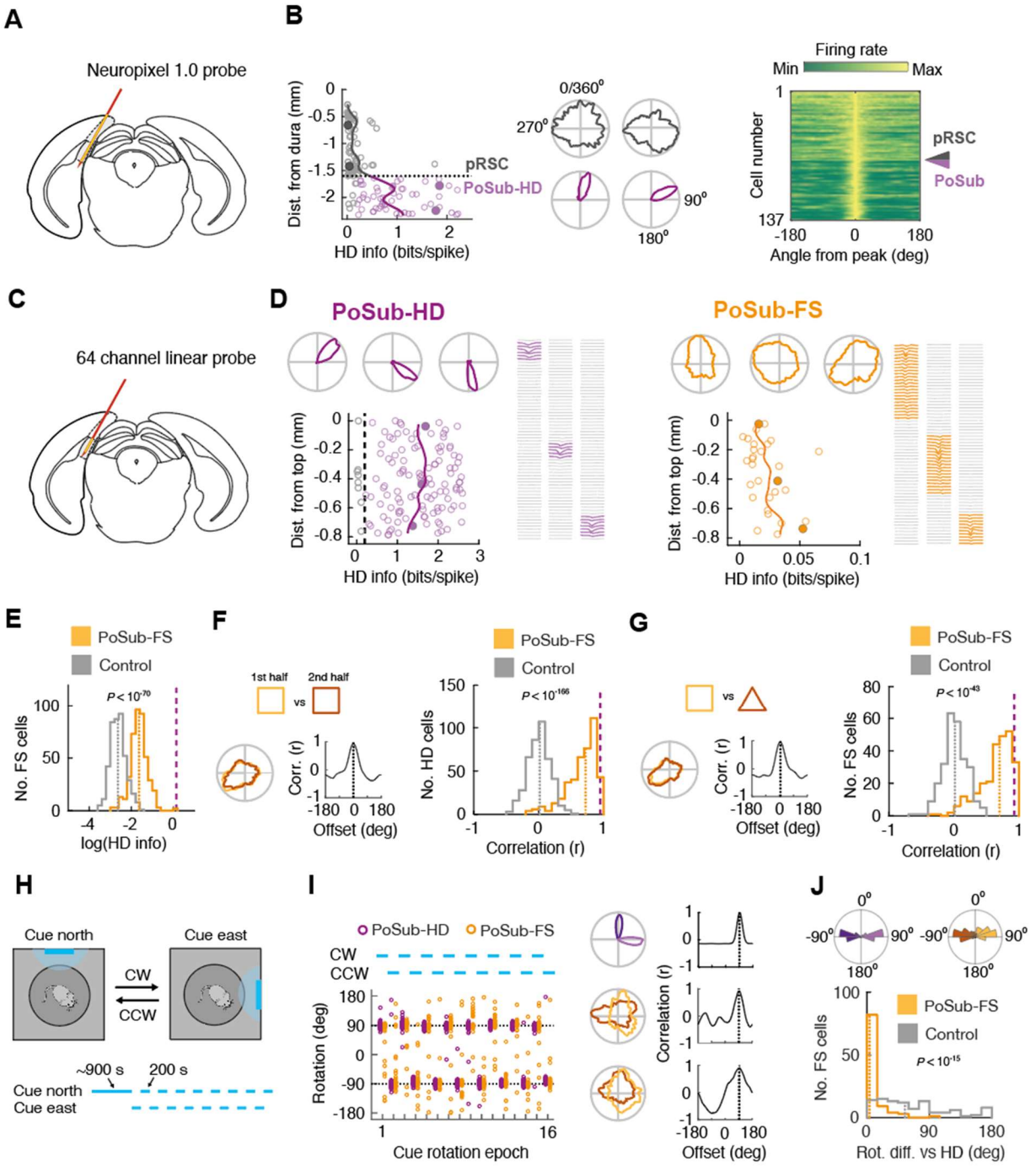

Figure 1. PoSub-FS cells share functional properties of canonical HD cells.

(**A**) Brain diagram showing the positioning of a Neuropixel probe along posterior retrosplenial cortex (pRSC) and PoSub.

(**B**) Left: Scatterplot depicting HD information of all putative excitatory cells in a single Neuropixel recording as well as the running average (continuous line). Representative HD tuning curves correspond to filled circles. Sudden appearance of sharply tuned HD cells (purple) at the depth of around 1.5 mm denotes

the putative boundary between pRSC and PoSub (dashed line). Right: Normalized tuning curves of all cells on the right, aligned to peak firing rate and sorted according to the position on the Neuropixel probe. The pRSC/PoSub boundary (arrowhead) is clearly identifiable.

(**C**) Brain diagram showing the angled positioning of the 64-channel linear probe right below the pRSC/PoSub boundary.

(**D**) Scatterplots depicting HD information of all putative excitatory cells (left) and putative FS cells (right) in a single angled 64-channel probe recording as well as the running average (solid lines). Representative HD tuning curves and waveforms correspond to filled circles.

(**E**) HD tuning of PoSub-FS cells (n = 427) carries more information than that of time-reversed controls (Wilcoxon signed rank test, $P < 10^{-70}$). Dotted lines show the medians of the depicted distributions, dashed line shows the median of the PoSub-HD cell distribution.

(**F-G**) PoSub-FS cells exhibit stable HD tuning between (**F**) two halves of a single recording epoch (n = 427; Wilcoxon signed rank test vs time-reversed control, $P < 10^{-166}$) as well as (**G**) between two recording epochs in arenas with different geometry (n = 264; Wilcoxon signed rank test vs time-reversed control, $P < 10^{-44}$). Left: representative tuning curve of a single PoSub-FS cell in two conditions and their circular cross-correlation. Dotted line shows the maximum correlation. Right: population histograms. Dotted lines show medians of the depicted distributions, dashed line shows the median of the PoSub-HD cell distribution.

(**H-J**) HD tuning of PoSub-FS cells is anchored to distal landmarks.

(**H**) Top: diagram of the cue rotation apparatus. The mouse was placed on a small elevated platform in a dim recording chamber, with the light from the distal cue providing the only light source. The cue was then rotated back-and-forth either clockwise (CW) or counterclockwise (CCW) by 90º every 200 seconds. Bottom: timeline of the epochs corresponding to different cue positions.

(**I**) Left: representative example of a single cue rotation session involving 16 consecutive cue rotation epochs (blue lines). Each point denotes the tuning rotation of a single cell relative to the previous epoch. Right: representative PoSub-HD and PoSub-FS tuning curves from the same session computed separately for CW and CCW epochs (light and dark shades, respectively), and their circular cross-correlation. Dotted line shows the maximum correlation.

(**J**) Top: Distribution of average tuning rotations of PoSub-HD cells (n = 411) and PoSub-FS cells (n = 99) across all CW and CCW epochs (light and dark shades, respectively). Bottom: Histogram of mean absolute rotation differences between individual PoSub-FS cells and PoSub-HD cells (n = 99, Wilcoxon signed rank test vs time-reversed control, $P < 10^{-15}$). Dotted lines show medians of the depicted distributions.

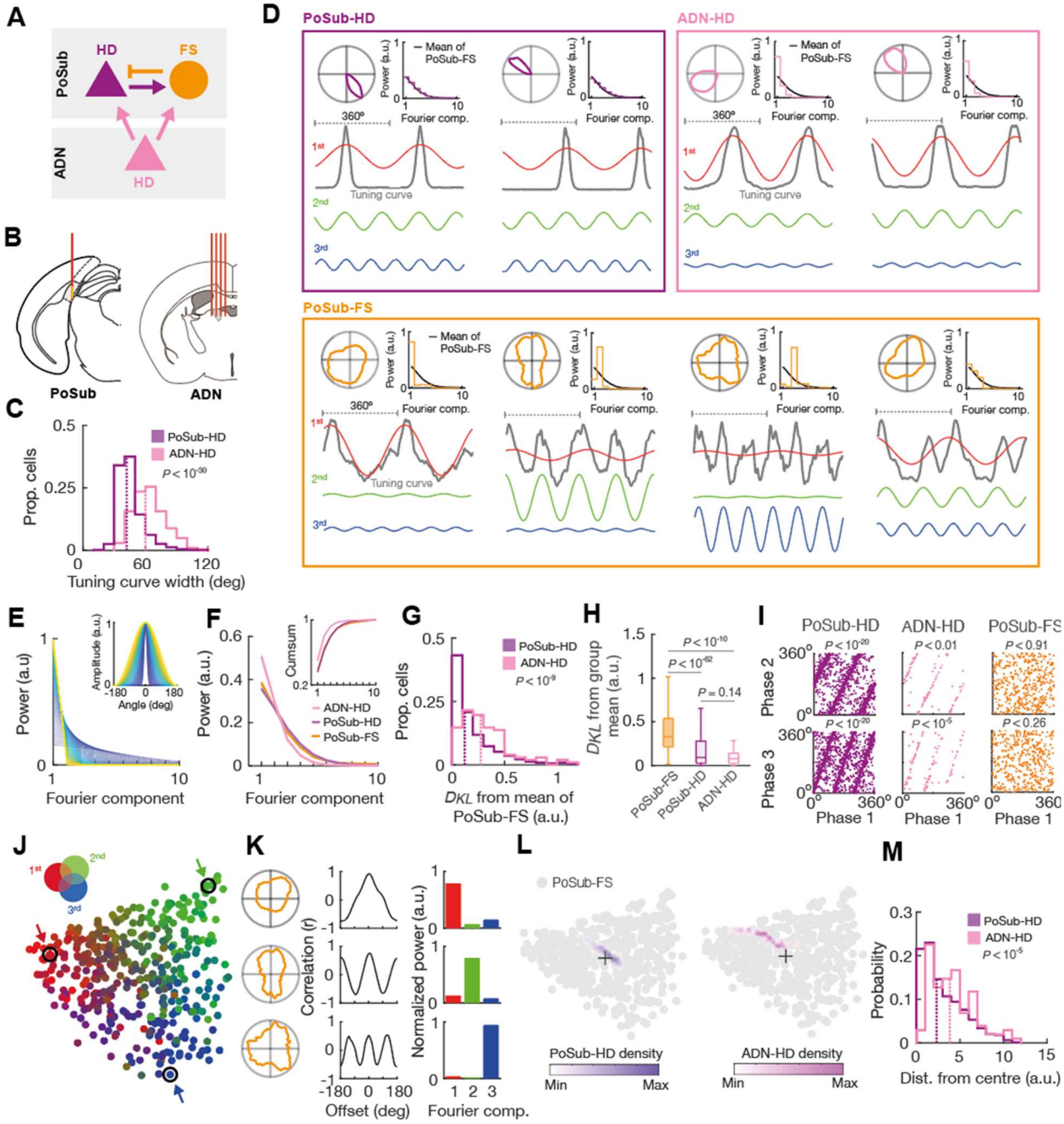

Figure 2. HD tuning of PoSub-HD and PoSub-FS cells is equivalent in the Fourier space.

(**A**) Simplified diagram of thalamocortical connections in the HD system.
(**B**) Brain diagram showing the positioning of probes in PoSub and the anterior thalamus.
(**C**) PoSub-HD cells have narrower tuning curves than ADN-HD cells (n = (1602, 97), Mann-Whitney U test, $P < 10^{-30}$). Dotted lines show the medians of the depicted distributions.
(**D**) Fourier decomposition of representative PoSub-HD ADN-HD and PoSub-FS HD tuning curves. Each example depicts the tuning curve in polar coordinates (top left), normalized power of first ten Fourier components (top right), and two periods of linearized tuning curve along with first 3 Fourier components. Black curves in Fourier spectra show the average PoSub-FS spectrum.

(**E**) Fourier spectra of simulated tuning curves as a function of tuning curve width. For wider tuning curves more power is concentrated in the first Fourier components. Inset: simulated tuning curves color-coded according to width.
(**F-G**) Average Fourier spectrum of PoSub-FS tuning curves reflects the average Fourier spectrum of PoSub-HD but not ADN-HD cells.
(**F**) Average Fourier spectra of PoSub-FS, PoSub-HD and ADN-HD cells (2-way ANOVA, Fourier component by cell type interaction: $P < 0.01$). Inset: cumulative distribution of the data in the main panel.
(**G**) ADN-HD cell Fourier spectra are further from the average PoSub-FS spectrum than the spectra of PoSub-HD cells (n = (1602, 97), Mann-Whitney U test, $P < 10^{-9}$). Dotted lines show the medians of the depicted distributions. D_{KL}, Kullback-Leibler divergence.
(**H**) PoSub-FS Fourier spectra are more widely distributed around their mean than those of HD cells (ANOVA, cell type, $P < 10^{-60}$). Individual comparisons (Bonferroni correction) displayed on the panel. D_{KL}, Kullback-Leibler divergence.
(**I**) The phases of Fourier components are correlated in PoSub-HD cells (circular correlation, Phase 1 vs Phase 2: $\rho_{cc} = 0.51$, $P < 10^{-20}$; Phase 1 vs Phase 3: $\rho_{cc} = 0.43$, $P < 10^{-20}$) and ADN-HD cells (circular correlation, Phase 1 vs Phase 2: $\rho_{cc} = 0.26$, $P < 0.01$; Phase 1 vs Phase 3: $\rho_{cc} = 0.44$, $P < 10^{-5}$) but not in PoSub-FS cells (circular correlation, Phase 1 vs Phase 2: $\rho_{cc} = 0.006$, $P = 0.91$; Phase 1 vs Phase 3: $\rho_{cc} = 0.06$, $P = 0.26$). ρ_{cc}, circular correlation coefficient.
(**J**) Two-dimensional Isomap projection of PoSub-FS cell tuning curve auto-correlograms reveals a continuous distribution of the first three Fourier components on the population level. Points represent auto-correlograms of individual PoSub-FS cells, coloured using the red-green-blue (RGB) colour model mapped to the relative power of the first 3 Fourier components. Arrows indicate examples shown in **K**.
(**K**) Representative PoSub-FS cell tuning curves (same as in **D**), their tuning curve auto-correlograms and the relative power of the first three Fourier components color-coded in RGB.
(**L**) Joint two-dimensional projection of PoSub-FS cell tuning curve auto-correlograms (gray points) and (left) PoSub-HD cell or (right) ADN-HD cell auto-correlograms. Values for PoSub-FS cell are shown as individual points (gray) underneath the density distribution of HD cell values. Densities below 0.1 of the maximum value are not shown. Black crosses indicate the centre of the PoSub-FS cell distribution.
(**M**) Euclidean distance to the centre of PoSub-FS distribution in **L**. PoSub-HD cells are more centered on the centre of PoSub-FS cell distribution than ADN-HD cells (Mann-Whitney U, $P < 10^{-9}$). Dotted lines show the medians of the depicted distributions.

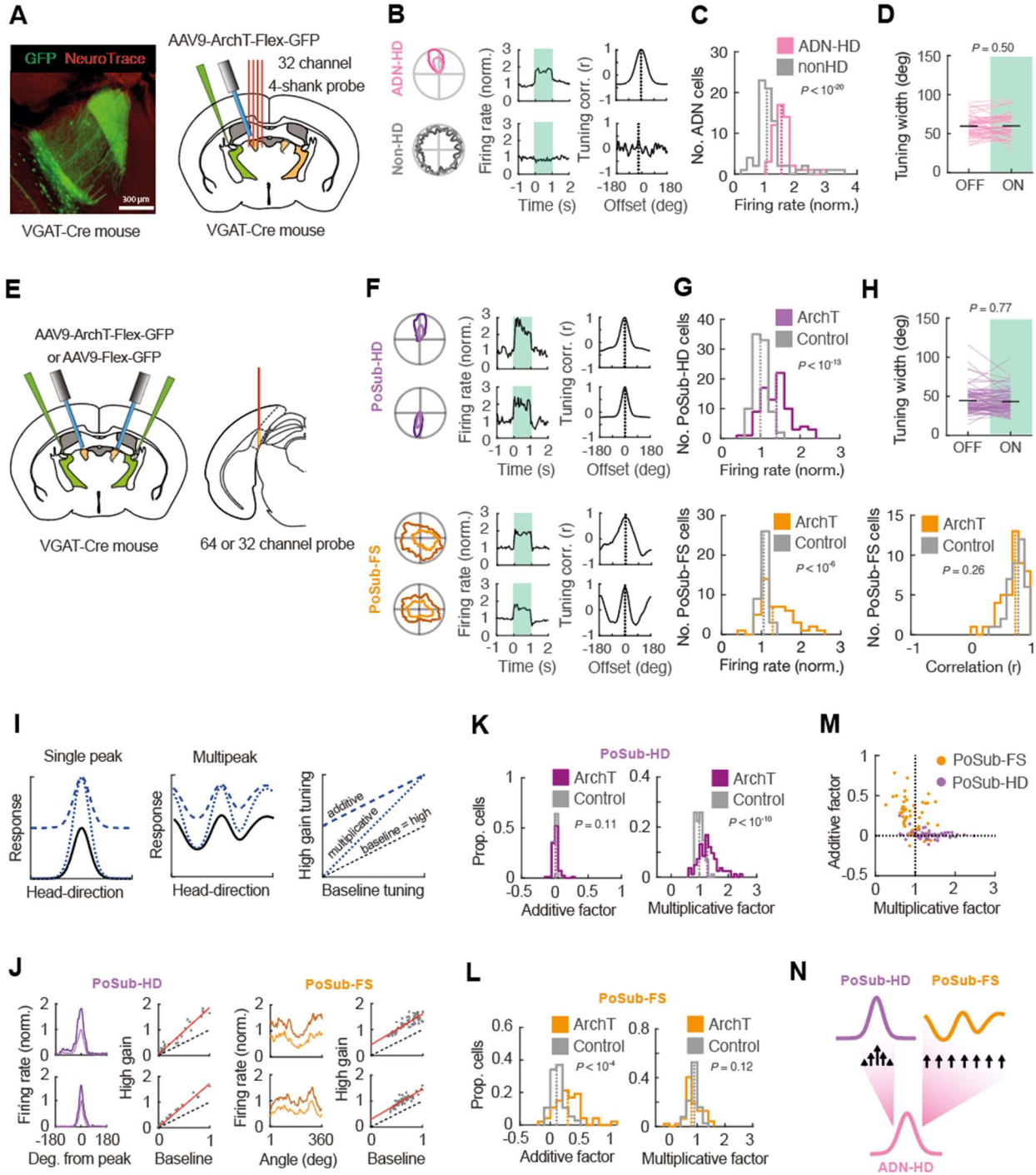

Figure 3: Thalamic drive provides uniform HD input to PoSub-FS cells.

(**A**) Optogenetic disinhibition of ADN. Left: Image of a coronal section from a VGAT-Cre mouse injected with a AAV9-Flex-GFP into anterior TRN, showing extensive putative inhibitory projections from TRN to ADN. Right: brain diagram of the unilateral viral injection into anterior TRN and positioning of the probe and optic fiber above ADN.

(**B-C**) Selective optogenetic modulation of thalamic HD gain.

(**B**) Representative examples of ADN-HD cell and thalamic non-HD cell responses to optogenetic inactivation of TRN projections to ADN. Left: HD tuning curves during light OFF epoch (light shades) and light ON epoch (dark shades). Middle: Average effect of the optogenetic manipulation on representative cells' firing rates. Green shading represents the duration of the light pulse. Right: cross-correlation between HD tuning curves during the light ON and light OFF epochs.
(**C**) Optogenetic inactivation of TRN input to ADN selectively increases the firing rate of ADN-HD cells without affecting thalamic non-HD cells (n = (52, 75), Mann-Whitney U test between cell types, $P < 10^{-20}$). Dotted lines show the medians of the depicted distributions.
(**D**) Optogenetic inactivation of TRN-ADN projections has no effect on the width of ADN-HD cell tuning curves (n = 52; Wilcoxon signed rank test, $P = 0.50$). Horizontal lines represent medians of each condition.
(**E**) Left: brain diagram of the bilateral viral injection into anterior TRN and positioning of optic fibers bilaterally above ADN. Right: brain diagram showing probe positioning in PoSub.
(**F-H**) Elevation of thalamic HD gain has no effect on HD tuning in PoSub.
(**F**) Representative examples of (top) PoSub-HD cell responses and (bottom) PoSub-FS cell responses to the optogenetic elevation of thalamic HD gain. Left: HD tuning curves for the light OFF epoch (light shade) and the light ON epoch (dark shade). Middle: Average effect of the optogenetic manipulation on representative cells' firing rates. Green shading represents the duration of the light pulse. Right: cross-correlation between HD tuning curves during the light ON and light OFF epochs.
(**G**) Elevation of thalamic HD gain increases the firing rates of both PoSub-HD cells (top; ArchT, n = 83; Control: n = 89; Mann-Whitney U test vs control group, $P < 10^{-13}$) and PoSub-FS cells (bottom; ArchT, n = 47; Control: n = 38; Mann-Whitney U test vs control group, $P < 10^{-6}$). Dotted lines show the medians of the depicted distributions.
(**H**) Top: Elevation of thalamic HD gain has no effect on the width of PoSub-HD cell tuning curves (n = 52; Wilcoxon signed rank test, $P = 0.50$). Horizontal lines represent medians of each condition. Bottom: elevation of thalamic HD gain has no effect on the HD tuning of PoSub-FS cells. Correlation of HD tuning curves during light ON and light OFF epochs (ArchT group, n = 47; Control group: n = 38; Mann-Whitney U test, $P = 0.26$). Dotted lines show the medians of the depicted distributions.
(**I-M**) Differential effect of thalamic gain modulation on HD and FS cells.
(**I**) Illustration of additive and multiplicative effects of gain modulation on (left) single-peaked and (right) multi-peaked tuning curves. Right: correlation between HD tuning curves in baseline conditions (black lines) and high gain conditions (blue lines) can reveal additive and/or multiplicative factors.
(**J**) Representative examples of PoSub-HD cells (left) and PoSub-FS cells (right) in baseline condition (light shades) and high gain condition (dark shades) plotted in Cartesian coordinates (same examples as in **F**) as well as their respective tuning correlation plots. Red lines represent the linear fit.
(**K**) Increase in the gain of thalamic HD input has a net multiplicative effect on HD tuning of PoSub-HD cells (Additive factor: Mann-Whitney U test vs Control group, $P = 0.11$; Multiplicative factor: Mann-Whitney U test vs Control group, $P < 10^{-10}$). Dotted lines show the medians of the depicted distributions.
(**L**) Increase in the gain of thalamic HD input has a net additive effect on HD tuning of PoSub-FS cells (Additive factor: Mann-Whitney U test vs Control group, $P < 10^{-6}$; Multiplicative factor: Mann-Whitney U test vs Control group, $P = 0.12$). Dotted lines show the medians of the depicted distributions.
(**M**) PoSub-HD and PoSub-FS cells form different clusters in the gain space.
(**N**) Diagram of differential effect of thalamic HD drive on PoSub-HD and PoSub-FS cells.

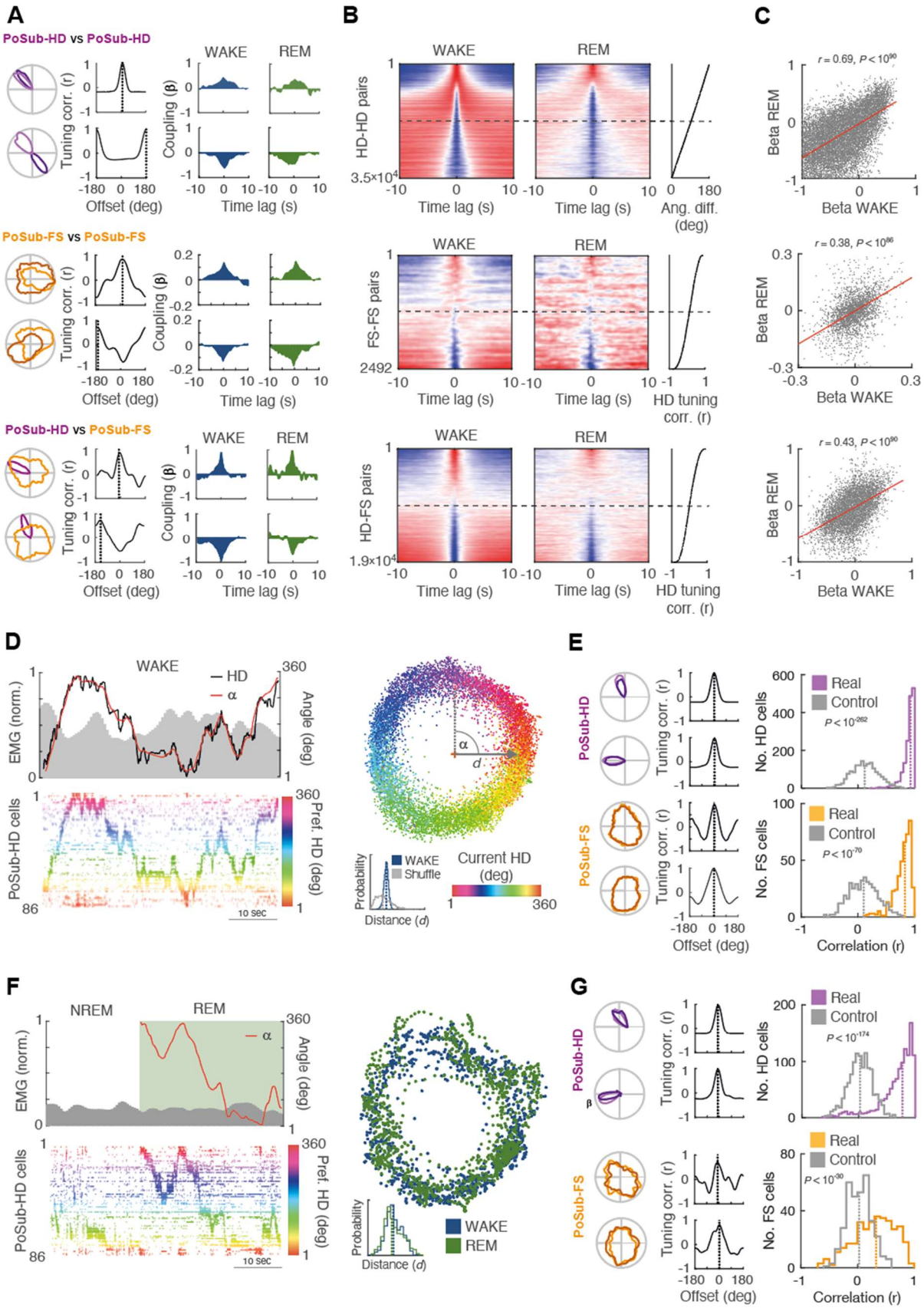
A
PoSub-HD vs PoSub-HD
WAKE
REM
Tuning corr. (r)
Coupling (β)
Offset (deg)
Time lag (s)
PoSub-FS vs PoSub-FS
PoSub-HD vs PoSub-FS
B
HD-HD pairs
FS-FS pairs
HD-FS pairs
Ang. diff. (deg)
HD tuning corr. (r)
C
Beta REM
Beta WAKE
D
EMG (norm.)
Angle (deg)
HD
α
PoSub-HD cells
Pref. HD (deg)
10 sec
Probability
WAKE
Shuffle
Distance (d)
Current HD (deg)
E
PoSub-HD
PoSub-FS
No. HD cells
No. FS cells
Real
Control
Correlation (r)
F
NREM
REM
G
β

Figure 4. PoSub-FS cells are coupled to local HD ring attractor dynamics.

(**A-C**) Spike-timing relationships of PoSub-HD:PoSub-HD cell pairs (top row), PoSub-HD:PoSub-FS cell pairs (middle row) and PoSub-FS:PoSub-FS cell pairs (bottom row).
(**A**) HD tuning and spike-timing relationships of representative cell pairs. Left: Superimposed HD tuning curves and their HD tuning cross-correlation. Dotted line shows the offset of maximum correlation. Right: GLM cross-coupling during WAKE and REM.
(**B**) Color-mapped GLM cross-coupling of all cell pairs during WAKE (left) and REM (middle). Cell pairs were sorted (right) according to the angular difference of their tuning curves (for PoSub-HD:PoSub-HD pairs) or tuning curve correlation at zero offset (PoSub-HD:PoSub-FS and PoSub-FS:PoSub-FS pairs). Each row represents a normalized cross-coupling curve of a single cell pair, color-mapped from minimum (blue) to maximum (red).
(**C**) Cross-coupling within and between PoSub-HD and PoSub-FS cell populations is preserved across WAKE and REM. Red line represents the linear fit.
(**D**) Isomap projection of HD cell population vectors during WAKE enables unsupervised reconstruction of HD from the 2-D ring manifold. Bottom left: HD cell raster plot of a 50 sec-long fragment of WAKE epoch from a single recording session. HD cells are sorted and colour-coded according to their preferred direction. Right: Isomap projection of HD population vectors during WAKE. Each point represents a single population vector, color-coded according to the animal's current HD. Coordinate α is the angular position of each population vector on the ring manifold. Distance of population vectors to the center of the manifold (d) is higher than that of the shuffled control. Top left: Coordinate α precisely matches the animal's current HD.
(**E**) Left: representative examples of PoSub-HD and PoSub-FS cell tuning curve reconstruction during WAKE using the coordinate α, and corresponding cross-correlograms between real HD tuning curves (light shades) and Isomap tuning curves (dark shades). Dotted line shows the offset of maximum correlation. Right: Isomap tuning curves during WAKE match HD tuning curves for both PoSub-HD cells (top; n = 1602; Wilcoxon signed rank test vs. time-reversed control, $P < 10^{-272}$) and PoSub-FS cells (bottom; n = 427; Wilcoxon signed rank test vs. time-reversed control, $P < 10^{-70}$).
(**F**) Isomap projection of HD cell population vectors during REM from the same recording session as in **D**. Bottom left: HD cell raster plot of a 50 sec-long fragment of a sleep epoch from a single recording session. HD cells are sorted and colour-coded according to their preferred direction during WAKE. Right: Isomap projection of HD population vectors during REM and WAKE (sub-sampled). Each point represents a single population vector. Distance of population vectors to the center of the manifold (d) is the same during WAKE and REM. Top left: Coordinate α represents the internal representation of direction during REM. Non-REM (NREM) epochs were not analyzed.
(**G**) Left: representative examples of PoSub-HD and PoSub-FS cell tuning curve reconstruction during REM using the coordinate α, and corresponding cross-correlograms between Isomap tuning curves during WAKE (light shades) and REM (dark shades). Dotted line shows the offset of maximum correlation. Right: Isomap tuning curves during REM match Isomap tuning curves during WAKE for both PoSub-HD cells (top; n = 1148; Wilcoxon signed rank test vs. time-reversed control, $P < 10^{-174}$ and PoSub-FS cells (bottom; n = 317; Wilcoxon signed rank test vs. time-reversed control, $P < 10^{-30}$).

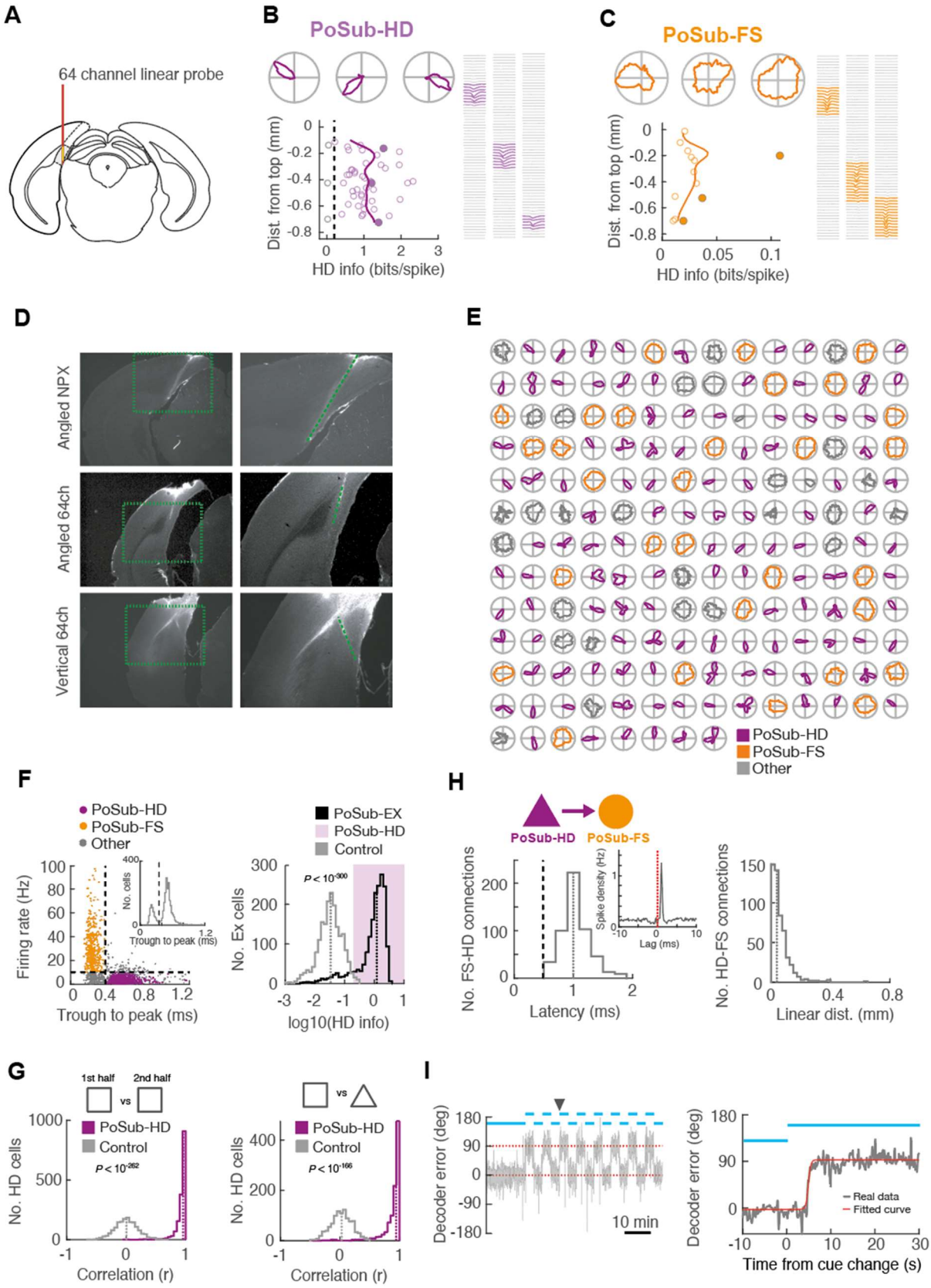
A
64 channel linear probe
B
PoSub-HD
Dist. from top (mm)
HD info (bits/spike)
C
PoSub-FS
Dist. from top (mm)
HD info (bits/spike)
D
Angled NPX
Angled 64ch
Vertical 64ch
E
PoSub-HD
PoSub-FS
Other
F
PoSub-HD
PoSub-FS
Other
Firing rate (Hz)
Trough to peak (ms)
No. cells
PoSub-EX
PoSub-HD
Control
No. Ex cells
log10(HD info)
H
PoSub-HD
PoSub-FS
No. FS-HD connections
Latency (ms)
Spike density (Hz)
Lag (ms)
No. HD-FS connections
Linear dist. (mm)
G
1st half
2nd half
PoSub-HD
Control
No. HD cells
Correlation (r)
I
Decoder error (deg)
10 min
Real data
Fitted curve
Time from cue change (s)

Supplementary Figure 1.

(**A**) Atlas diagram showing the vertical positioning of the 64-channel linear probe in PoSub.
(**B-C**) Scatterplot depicting HD information of all putative excitatory cells (**B**) and putative FS cells (**C**) in a single vertical 64-channel probe recording as well as the running average (solid lines). Representative HD tuning curves and spike waveforms correspond to filled circles.
(**D**) Anti-mouse antibody-stained coronal sections depicting the probe tract for the Neuropixel recording (top) as well as representative tracts for the angled (middle) and vertical recordings (bottom). Images on the right are magnified regions denoted on the left. Dashed line, position of the probe recording sites.
(**E**) HD tuning curves of all cells recorded in the session depicted in Figure 1B-C, arranged in anatomical order from dorsal to ventral.
(**F**) Identification of cell types. Left: units were separated into putative EX and FS cells based on firing rate and waveform shape (dashed lines). Left, inset: bimodal distribution of trough-to-peak duration in the recorded PoSub cell population. Right: HD tuning of PoSub-EX cells (n = 1835) carries more information than that of time-reversed controls (Wilcoxon signed rank test, $P < 10^{-300}$). A sub-population of PoSub-EX cells with HD information higher than 99th percentile of the time-reversed control population was classified as PoSub-HD cells. Dotted lines show the medians of the depicted distributions.
(**G**) PoSub-FS cells receive inputs from local PoSub-HD cells. Left: Latency of identified synaptic connections. Dashed line depicts the latency threshold. Left, inset: example spike timing cross-correlogram between a PoSub-HD and a PoSub-FS cell showing a putative synaptic connection. Right: linear distance between putative synaptic partners. Dotted lines show the medians of the depicted distributions.
(**H**) PoSub-HD cells exhibit stable HD tuning between (left) two halves of a single recording epoch (n = 1602; Wilcoxon signed rank test vs time-reversed control, $P < 10^{-262}$) as well as (right) between two recording epochs in arenas with different geometry (n = 1013; Wilcoxon signed rank test vs time-reversed control, $P < 10^{-166}$). Dotted lines show medians of the depicted distributions.
(**I**) Angular error of the Bayesian decoder during a representative cue rotation session. Left: rotation of the cue by 90 degrees reliably corresponds to the equivalent error in HD decoding. Right: changes in decoder error during a single cue rotation epoch (denoted with a black arrowhead in right). Red line is the sigmoidal function fitted to estimate the end of remapping. Blue bars denote changes in cue position.

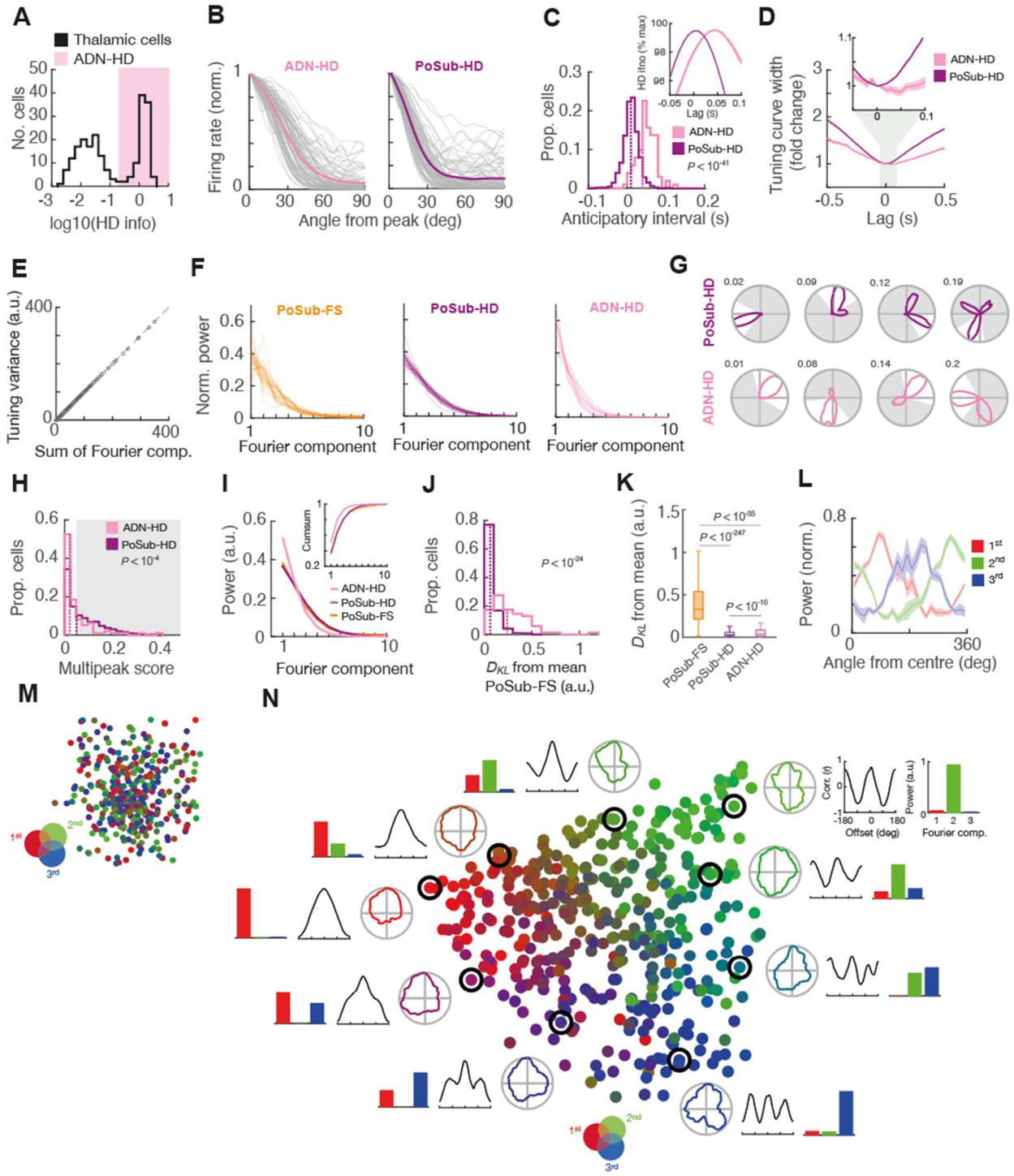

Supplementary Figure 2.

(A) Cells recorded in the anterior thalamus show bimodal distribution of HD information. Pink background denotes classified ADN-HD cells (n = 97), the threshold of 0.2 bits/spike is the same as that used to classify PoSub-HD cells.

(**B**) Tuning curve slopes of ADN-HD cells (n = 97) and PoSub-HD cells (n = 97, randomly selected). Thin gray lines denote individual tuning curves, thick coloured lines denote averages of depicted populations.
(**C-D**) Differences in tuning curve width between ADN-HD and PoSub-HD cells are not due to differences in anticipatory intervals.
(**C**) Distribution of anticipatory intervals for ADN-HD and PoSub-HD cells. Mann-Whitney U test, n = (1602, 97l), $P < 10^{-41}$). Dotted lines show the medians of the depicted distributions. Inset: change in HD information as a function of time lag. Shaded lines represent mean +/- SEM.
(**D**) Negligible decrease in tuning width of ADN-HD cells after correcting for the anticipatory interval.
(**E**) Fourier decomposition of HD tuning curves obeys Parseval's identity, with the sum of all Fourier components equal to the variance of the tuning curve.
(**F**) Average Fourier spectra of PoSub-FS, PoSub-HD and ADN-HD cells per animal.
(**G-K**) Identification of multipeaked HD cells and their effect on the average Fourier spectra.
(**G**) Examples of HD tuning curves of PoSub-HD and ADN-HD cells along with their multipeak score. Shaded areas of the tuning curves represent the regions outside of the primary receptive field.
(**H**) Distribution of the multipeak score in PoSub-HD and ADN-HD cells. PoSub-HD cells tend to have a higher multipeak score than ADN-HD cells (Mann-Whitney U test, n = (1602, 97l), $P < 10^{-4}$). Shared area denotes cells excluded form further analysis. Dotted lines show the medians of the depicted distributions.
(**I**) Average Fourier spectra of PoSub-FS cells (n = 427), PoSub-HD cells (n = 789) and ADN-HD cells (n = 69) after exclusion of multipeaked HD cells (2-way ANOVA, Fourier component by cell type interaction: $P < 10^{-4}$). Inset: cumulative distribution of the data in the main panel.
(**J**) After exclusion of multipeaked HD cells ADN-HD cell Fourier spectra are still further from the average PoSub-FS spectrum than the spectra of PoSub-HD cells (Mann-Whitney U test, n = (789, 69), $P < 10^{-24}$). Dotted lines show the medians of the depicted distributions. D_{KL}, Kullback-Leibler divergence.
(**K**) PoSub-FS Fourier spectra are more widely distributed around their mean than those of HD cells (ANOVA, cell type, $P < 10^{-246}$). Individual comparisons (Bonferroni correction) displayed on the panel. D_{KL}, Kullback-Leibler divergence.
(**L**) Relative power of first three Fourier components changes as a function of the angular coordinate from the centre of tuning curve autocorrelogram Isomap projection (**Figure 2J**).
(**M**) Two-dimensional Isomap projection of time-reversed control PoSub-FS cell tuning curve auto-correlograms does not map onto their Fourier spectra. Points represent auto-correlograms of individual PoSub-FS cells, coloured using the red-green-blue (RGB) colour model mapped to the relative power of the first 3 Fourier components.
(**N**) Additional representative PoSub-FS cell tuning curves, their tuning curve auto-correlograms and the relative power of the first three Fourier components color-coded in RGB, mapped onto the Isomap projection of PoSub-FS cell tuning curve auto-correlograms. Points represent auto-correlograms of individual PoSub-FS cells, coloured using the red-green-blue (RGB) colour model mapped to the relative power of the first 3 Fourier components. Tuning curves of PoSub-FS cells are colour-coded accordingly.

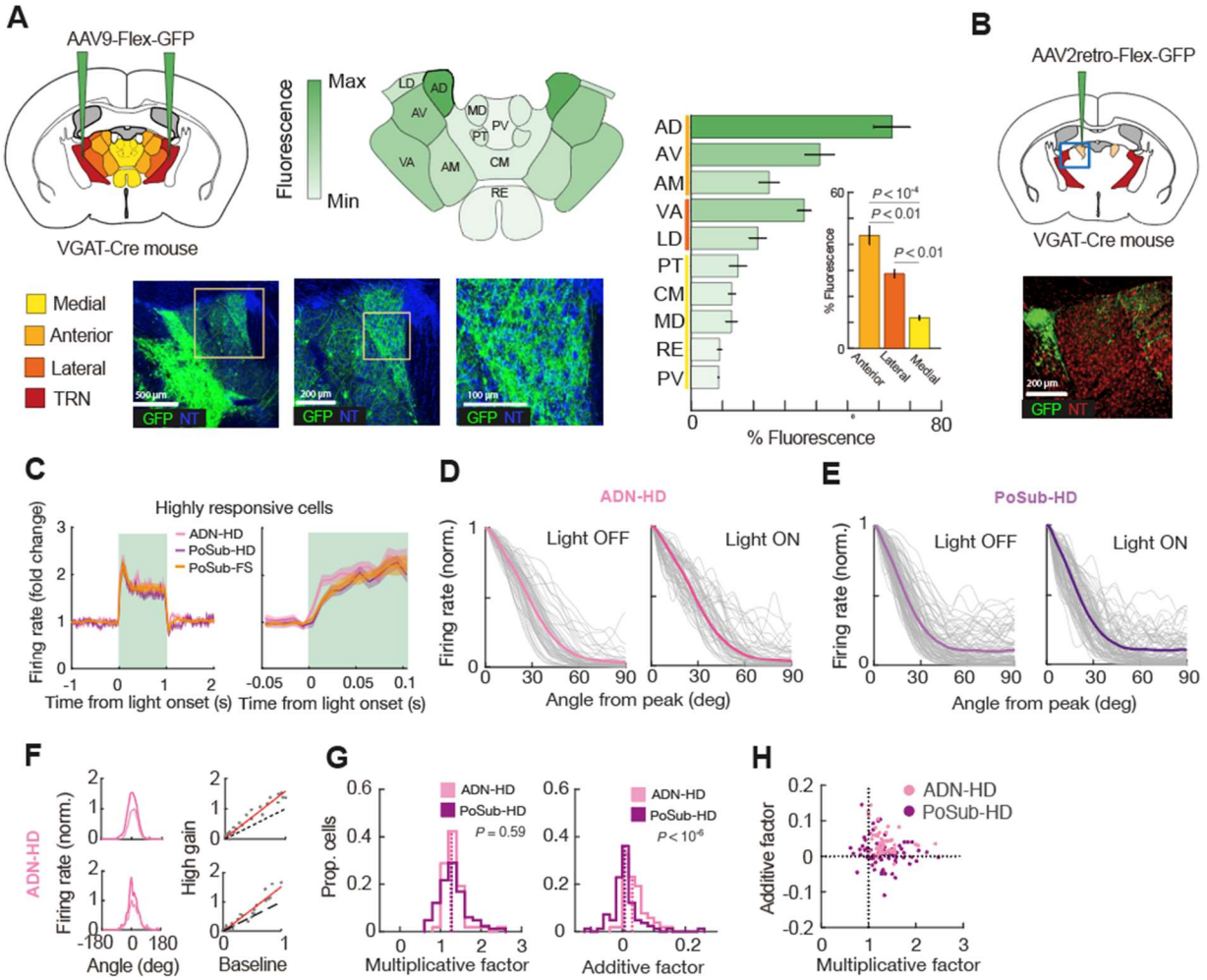

Supplementary Figure 3.

(**A**) Anterograde tracing of projections from TRN to the rostral thalamus. Top left: coronal diagram showing virus injection sites and sub-divisions of the rostral thalamic nuclei. Bottom: representative images of fluorescent signal in TRN and neighbouring thalamic nuclei. Left: ADN has the highest density of TRN axonal projections among rostral thalamic nuclei (n = 4 mice). Left inset: density of TRN projections across sub-divisions of the rostral thalamus (repeated measures ANOVA, $F_{(2,9)} = 44.9$, $P < 10^{-4}$). Individual comparisons (Bonferroni correction) displayed on the panel. Data shown as mean +/- SEM. Top: individual rostral thalamic nuclei colour-coded according to the TRN projection strength. AD, anterodorsal nucleus; AV, anteroventral nucleus; AM, anteromedial nucleus; VA, ventral anterior nucleus; LD, laterodorsal nucleus; PT, paratenial nucleus; CM, centromedial nucleus; MD, mediodorsal nucleus; RE, nucleus reuniens; PV, paraventricular nucleus.
(**B**) Retrograde tracing of projections from TRN to ADN. Top: coronal diagram showing the virus injection site. Bottom: representative image of fluorescent signal in ADN and anterodorsal TRN.
(**C**) Temporal profile of ADN-HD, PoSub-HD and PoSub-FS responses to optogenetic ADN disinhibition. Left: Average response of highly-responsive cells is similar across the three populations. Only the cells with average response above the median for a given population were included (n = 26, 41, 23). Right: ADN-HD cells respond to light pulses at shorter latency than PoSub cells.

(**D**) Tuning curve slopes of ADN-HD cells (n = 52) during light ON and light OFF epochs. Thin gray lines denote individual tuning curves, thick coloured lines denote averages of depicted populations.
(**E**) Tuning curve slopes of PoSub-HD cells (n = 83) during light ON and light OFF epochs. Thin gray lines denote individual tuning curves, thick coloured lines denote averages of depicted populations.
(**F**) Representative examples of ADN-HD cells in baseline condition (light shades) and high gain condition (dark shades) plotted in cartesian coordinates as well as their respective tuning correlation plots. Red lines represent the linear fit.
(**G**) Inactivation of TRN input has a similar multiplicative effect on ADN-HD cells as on PoSub-HD cells (Mann-Whitney U test, $P = 0.58$) but ADN-HD cells additionally show a modest amount of additive gain (Mann-Whitney U test, $P < 10^{-6}$). Dotted lines show the medians of the depicted distributions.
(**H**) ADN-HD and PoSub-HD cells form overlapping clusters in the gain space.

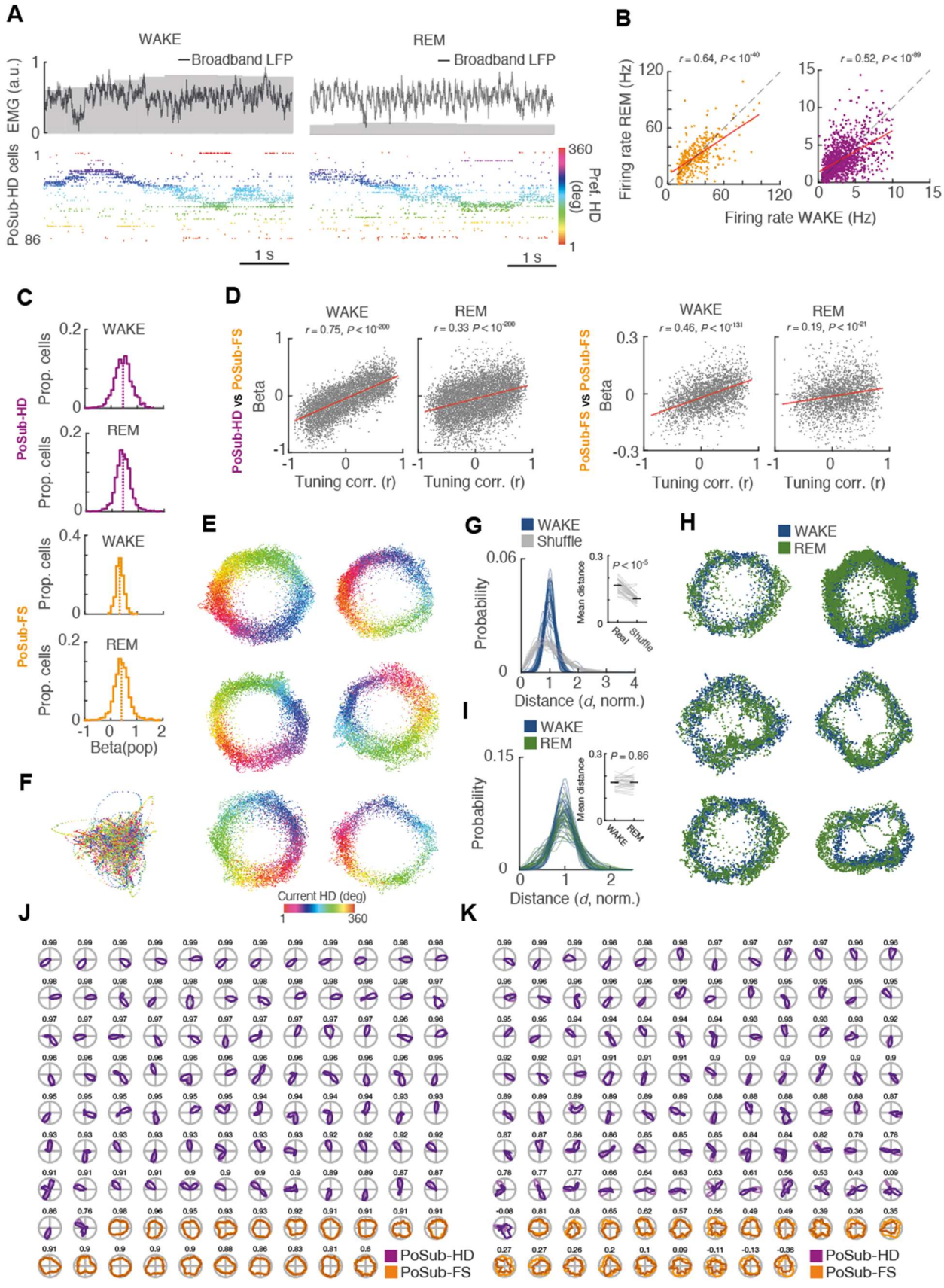
A
WAKE
REM
Broadband LFP
EMG (a.u.)
PoSub-HD cells
Pref. HD (deg)
1 s
B
r = 0.64, P < 10^-40
r = 0.52, P < 10^-89
Firing rate REM (Hz)
Firing rate WAKE (Hz)
C
PoSub-HD
PoSub-FS
Prop. cells
Beta(pop)
D
PoSub-HD vs PoSub-FS
Beta
Tuning corr. (r)
r = 0.75, P < 10^-200
r = 0.33 P < 10^-200
r = 0.46, P < 10^-131
r = 0.19, P < 10^-21
E
F
G
WAKE
Shuffle
Probability
Distance (d, norm.)
Mean distance
P < 10^-5
Real
Shuffle
H
REM
I
P = 0.86
WAKE
REM
Current HD (deg)
J
K
PoSub-HD
PoSub-FS

Supplementary Figure 4.

(**A**) Representative LFP traces and PoSub-HD cell raster plots during WAKE and REM epochs. Grey areas indicate level of LFP-derived electromyogram (EMG, see Methods).
(**B**) Significant Pearson correlations between mean firing rates during WAKE and REM epochs for both PoSub-HD and PoSub-FS cells.
(**C**) GLM coupling of individual cells to the population firing rate.
(**D**) Scatter plots showing significant Pearson correlations between HD tuning and GLM pairwise coupling (Beta) for PoSub-HD:PoSub-FS and PoSub-FS:PoSub-FS cell pairs across during both WAKE and REM epochs.
(**E**) Additional examples of Isomap projections of HD population vectors during WAKE from six different recordings.
(**F**) Example of the Isomap projection of shuffled HD population vectors (same recording as in Figure 4D)
(**G**) Distribution of distance values to the centre of the manifold for all WAKE Isomap projections of real and shuffled HD population vectors, normalized to the mean distance of the real projections. Inset: mean distance to the centre of the manifold for real Isomap projections (n = 32 mice) is significantly higher than in shuffled controls (Wilcoxon signed rank test, $P < 10^{-5}$).
(**H**) Additional examples of Isomap projections of HD population vectors during WAKE and REM from six different recordings (same animals as in E).
(**I**). Distribution of distance values to the centre of the manifold for all REM and subsampled WAKE Isomap projections, normalized to the mean distance of the WAKE projections. Inset: mean distance to the centre of the manifold for REM and subsampled WAKE Isomap projections (n = 26 mice) (Wilcoxon signed rank test, $P = 0.86$).
(**J**) Real HD tuning curves (light shades) and Isomap-generated HD tuning curves (dark shades) of all PoSub-HD and PoSub-FS cells from a single recording (same as in Figure 2D).
(**K**) Isomap-generated HD tuning curves during WAKE (light shades) and REM (dark shades) of all PoSub-HD and PoSub-FS cells from a single recording (same as in Figure 2F).

Methods

Subjects

All procedures were approved by the Animal Care Committee of the Montreal Neurological Institute at McGill University in accordance with Canadian Council on Animal Care guidelines. The subjects were adult (> 8 week old) mice bred by crossing wild-type females on C57BL/6J background (Jackson laboratories 000664) with either homozygous male VGAT-IRES-Cre mice (Jackson laboratories 028862, n = 36) or PV-IRES-Cre mice (Jackson laboratories 017320, n = 3). An addition mouse implanted with a Neuropixel probe (**Figure 1A,B**) was a cross-bred C57BL/6J and FVB (Jackson laboratory 001800). Mice were kept on a 12 hour light/dark cycle and were housed in group cages (2 – 5 mice per cage) before electrode implantation surgery and individually afterwards. A summary of behavioural protocols undergone by each mouse as well as dataset assignments can be found in Table S1.

Electrode implantation

C57BL/6 mice (Jackson Laboratory) were implanted under isofluorane anaesthesia, as previously described [14]. Briefly, silicon probes were mounted on in-house build movable microdrives and implanted through a small craniotomy. Probes were implanted either vertically above left PoSub (from Bregma: AP, -4.24 mm; ML, 2.05 mm; DV, -1.00 mm) or at a 26 degree angle pointing away from the midline into left posterior retrosplenial cortex (from Bregma: AP, -4.24 mm; ML, 1.70 mm; DV, -1.00 mm). A mesh wire cap was then build around the implanted microdrive and was reinforced with UV-cured adhesive. Mice were allowed to recover for at least 3 days before electrophysiological recordings.

The probes consisted of either a Neuropixel 1.0 probe (384 active sites arranged in a dense checkerboard layout, i.e. two columns, 20 µm between each row), a single shank with 64 recording sites (H5, Cambridge Neurotech, electrodes staggered in two rows, 25 µm vertical separation) or 4 shanks with 8 recording sites each (Buzsaki32, Neuronexus, electrodes staggered in two rows, 20 µm vertical separation). In all experiments both ground and reference wires were soldered to a single 100 µm silver wire which was then implanted 0.5 mm into the cerebellum.

Recording procedures

During the recording sessions, neurophysiological signals were acquired continuously at 20 kHz on a 256 channel RHD USB interface board (Intan Technologies). The wide-band signal was downsampled to 1.25 kHz and used as the LFP signal. The animals were tethered to a motorized electrical rotary joint (AERJ, Doric Lenses) in order to enable free movement around the enclosure. Ahead of the main recording session, the microdrive was lowered over several hours in small (35 - 70 µm) increments until the whole shank was positioned in PoSub or ADN. A short open field session was then recorded in order to map the HD receptive fields of all neurons. For PoSub, the

recording depth was adjusted so that sharply-tuned HD cells (a hallmark of PoSub) are present along the whole length of the shank. Data collection did not commence until at least 2 hours after the last depth adjustment. Only one recording session per mouse was included in the analysis in order to prevent double counting of cells.

Animal position and orientation was tracked in 3D using 7 infrared cameras (Flex 13, Optitrack) placed above the enclosure and coupled to the Optitrack 2.0 motion capture system. Five small tracking markers were attached to the headcap and additional 2 larger markers were attached to the amplifier chip. In addition, video recording was captured by an overhead camera (Flex 13, Optitrack) placed close to the rotary joint. Animal position and head orientation was sampled at 100 Hz and was synchronized with the electrophysiological recording via TTL pulses registered by the RHD USB interface board (Intan). The tracking system was calibrated in the same manner across all recording sessions to ensure that the tracking coordinates were the same across the whole dataset.

Behavioural procedures

Before the implant surgery, mice were habituated over several days to forage for small pieces of Honey Cheerios cereal (Nestle) in the open field. For most recordings, the recording chamber consisted of a metal frame (90 x 90 x 180 cm) supporting a plastic platform with removable walls (width: 80 cm, height: 50 cm) that could be arranged into either a square or triangular open field. The recording protocol consisted of a sleep session in the home cage, followed by open field exploration in a square arena and another sleep session. A subset of animals then explored a triangular arena. A white rectangular cue card on one of the walls served as a salient cue. Both environments were oriented so that the wall with the cue card always faced the same direction.

Optogenetic experiments

Mice were injected with an adeno-associated virus vector (AAV 2/9 CAG-Flex-ArchT-EGFP or CAG-Flex-EGFP, titer: 4-5 x 10^{12} GC/ml, Neurophotonics) into the thalamic reticular nucleus (from Bregma: AP, -0.70 mm; ML, 1.25 cm; DV, -3.25 cm) under isofluorane anasethesia either unilaterally for ADN recordings or bilaterally for PoSub recordings. Injections (300-400 nl per injection site) were done with a microinjector (Harvard Apparatus and Nanofil syringe) through a small craniotomy, at the speed of 100 nl/s. The needle was left in place for 2-5 min after injection in order to minimize backflow.

After at least 3 weeks since the injection surgery, optic fiber implants (Doric Lenses, MFC_200/240-0.22_25mm_SM3) were implanted unilaterally (left hemisphere, ADN recordings) or bilaterally (PoSub recordings) above ADN at a 20-degree angle from the sagittal plane (from Bregma: AP, -0.82 mm; ML, 1.00 cm; DV, -2.25 cm). Mice were then implanted with a microdrive-mounted Buzsaki32 probe above left ADN (Bregma: AP, -0.82 mm; ML, 0.85 cm; DV, -2.00 cm) or either Buzsaki32 or H5 probe above left PoSub, as described above.

Laser light was delivered from a 520 nm fiber-coupled laser diode module (Doric Lenses) controlled with a laser diode module driver (Doric Lenses). Light power output at the tip of the fiber implant was measured before each implantation and a dose-response curve was calculated individually for each implant. Light output was then set to 14-16 mW before each recording session. For this subset of mice, the second sleep session was followed by a second exploration session in the open field, during which a laser stimulation protocol was delivered via patch cords attached to the optic fiber implants. After 5 min of exploration, light pulses (1 s) were delivered at 0.2 Hz in groups of 60 (5 min total), each followed by 5 min of no stimulation. Four such epochs were delivered in total, resulting in 240 light pulses over a 45 min recording session. Such short and interspersed pulses were chosen to promote even sampling of the animal's current orientation and minimize overheating of the brain.

For animals implanted with single-shank linear probes, only one session per mouse was included in the analysis in order to prevent double-counting of cells. For animals implanted with 4-shank Buz32 probes, multiple sessions per mouse (obtained on separate days) were included in the analysis, ensuring that the probe was moved by at least 70 μm between the recording sessions.

Cue rotation experiment

A subset of animals implanted into PoSub with linear H5 probes underwent a cue rotation experiment in a separate recording session. To this end, the frame of the recording chamber was fitted with black plastic insets that covered the floor (90 x 90 cm) and walls in order to hide any visual cues. Additionally, the outside of the recording chamber was covered with thick fabric in order to block off any light coming from the outside. Each of the four walls had an identical panel made of two LED strips (yellow V-shape or blue X-shape) in the centre. A small (30 cm diameter) elevated circular platform was placed in the centre of the arena, at the elevation corresponding to the bottom of the LED panels. Before each recording session, two adjacent LED panels were chosen as distal visual cues. The LED light intensity was chosen so that the panels are visible in the dark but provide minimal illumination of the surrounding area. The on/off cycle of the LED panels was controlled with an Arduino computer. In order to eliminate other sensory cues, the whole recording chamber was thoroughly cleaned with antibacterial wipes before the experiment and white noise was emitted from speakers placed underneath the chamber, below the circular platform.

The recording protocol consisted of a 1-hour sleep session in the home cage placed on the circular platform, followed by a 75 min cue rotation session. At the start of the cue rotation session a single LED cue dimly illuminated, the mouse was placed directly on the circular platform and was left undisturbed for the duration of the session. The recording chamber was then sealed to ensure near-complete darkness except for the dimly illuminated LED cue. After 15-20 min of exploration with a stable cue, the cue rotation protocol was initiated. The protocol consisted of the illuminated cue

switching 8 times back and forth between two adjacent walls (16 total cue rotations), each time staying in place for 200s. Additionally, in order to habituate the mouse to the cue disappearing from its field of view, the cue was turned off for 0.1 s every 20 s. In order to encourage the mouse to explore the platform for the whole duration of the session, the experiment was conducted in the middle of the dark phase of the light cycle and the recording chamber was sprayed with a novel odour (scented air freshener) right before the cue rotation session.

Tissue processing and probe recovery

Following the termination of the experiments, animals were deeply anesthetized and perfused transcardially first with 0.9% saline solution followed by 4% paraformaldehyde solution. The microdrive was then advanced to remove the probe from the brain and the probe was moisturized with distilled water while the brain was being extracted. Brains were sectioned with a vibratome sagitally in 40 μm thick slices. Sections were washed, counterstained with DAPI and Red Neurotrace and mounted on glass slides with ProlongGold fluorescence antifade medium. Sections containing probe tracts were additionally stained with a Cy3 anti-Mouse secondary antibody to help visualize the electrode tract. Widefield fluorescence microscope (Leica) was used to obtain images of sections and verify the tracks of silicon probe shanks, optic fiber position and virus expression.

Probes were lifted out of the brain immediately after perfusion by turning the Microdrive screw all the way up. As the headcap was being manually dismantled, the probe shank was then kept from drying by infusions of distilled water into the headcap. Once the drive-mounted probe was separated from the headcap, it was immersed in 3% peroxide for 5 minutes and rinsed with distilled water. The probe was then dipped in and out of a warm Contrad solution for several minutes, followed by a 2-hour incubation in a warm 2% Tergazyme solution. The drive-mounted probe was then rinsed with distilled water and stored for the next implantation. This multistep cleaning protocol enabled us to implant an individual probe an average of 3 times.

Spike sorting and unit classification

Spike sorting was performed semi-automatically, using Kilosort 2.0 [62] followed by manual curation of the waveform clusters using the softwares Klusters [63] and Phy [64]. At this stage, any cluster without a clear waveform and clear refractory period in the spike train autocorrelogram were classified as noise and cluster pairs with similar waveforms and common refractory period in their spike train cross-correlogram were merged.

For PoSub recordings, viable units were first identified as units that (1) had an average firing rate of at least 0.5 Hz during open field exploration, and (2) had a waveform with negative deflection (criterion aiming to exclude spikes from fibers of passage). Next, putative excitatory cells and putative FS interneurons were classified on the basis of their mean firing rate during open field exploration and the through-to-peak duration of their average waveforms (Figure S1F). Putative FS interneurons were defined as cells with short trough to peak duration (< 0.38 ms) and high

mean firing rates (> 10 Hz). Conversely, cells with long trough-to-peak (>0.38 ms) and low mean firing rates (< 10 Hz) were classified as putative excitatory cells.

HD tuning curves and tuning metrics

The animal's HD was calculated as the horizontal orientation of a polygon constructed in Optitrack from the 3-dimensional coordinates of all tracking markers, relative to the global coordinates, constant across the whole study (see above). In order to minimize the effect of animal's velocity on HD tuning curves, the dataset was limited to the epochs when animal's speed exceeded 2 cm/s for all analyses except cue rotation and optogenetic experiments, where epoch duration (200 and 240 s, respectively) was too short to warrant further refinement. HD tuning curves were then computed as the ratio between histograms of spike count and total time spent in each direction in bins of 1 degree and smoothed with a Gaussian kernel of 3° s.d.

Since a sizable proportion of HD cells in our dataset had tuning curves with multiple peaks and therefore low resultant vector lengths, we chose to define HD cells based on a HD information [65], calculated for N angular bins as: $I = \sum_{i=1..N} \lambda(\Theta_i)\, log_2\left(\frac{\lambda(\Theta_i)}{\lambda}\right)\, p(\Theta_i)$

where $\lambda(\Theta_i)$ is the firing rate of the cell for the *i*th angular bin, λ is the average firing rate of the neuron during exploration and $p(\Theta_i)$ is the occupancy (i.e. normalized time spent) in direction Θ_i.

For each cell, we obtained the control tuning curve by computing a tuning curve using time-reversed HD angle – a method that preserves the dynamics of both the spike train and the HD angle but decouples the two from each other. We then classified HD cells as those with HD information scores higher than 99th percentile of the null distribution (> 0.2 bits/spike, 85% of putative excitatory cells).

Similarly, we used HD information (see above) to characterize the HD tuning of FS cells. Should we apply our HD cell definition to the recorded putative FS cells, 67% of FS cells would pass the 99th percentile of the null distribution (> 0.015 bit/spike). However, since the vast majority of recorded FS cells had stable HD tuning across the recording session (**Figure 1F,G**), we decided to include all recorded FS cells in the subsequent analyses.

Cross-validated HD tuning curve auto- and crosscorrelograms

We obtained HD tuning curve auto- and crosscorrelograms by computing Pearson's correlation coefficients between the reference tuning curve vector and the second tuning curve vector (from either the same or another cell), which was circularly shifted by 0 to 359 bins. In order to minimize the effect of non-HD factors on tuning curves computed from the same epoch, we employed a cross-validation procedure whereby the two tuning curves were computed from separate halves of the epoch.

When computing the HD tuning curves during exploration of the triangular open field, we have noticed that sometimes the cells' receptive fields were rotated with respect to the prior square open

field exploration. In order to counteract this, we first calculated for each HD cell the degree of tuning curve rotation between the two environments via cross-correlation. We then used the average rotation value per recording session to circularly shift all triangular open field tuning curves in the opposite direction by the equivalent amount. This allowed us to compute the true tuning curve correlation between the two environments.

Analysis of HD cell realignment after cue rotation

In order to estimate the degree of realignment of the HD system following cue rotation, the 'internal' HD was reconstructed using a Bayesian framework following previous work [14,66]. In short, HD cell spike times were binned into population vectors (50 ms window, smoothened in 100 ms s.d. Gaussian windows). Based on cells' tuning curves from the period of exploration with stable cue, the population vectors were converted into a probabilistic map under the hypothesis that HD cells fire as a Poisson process. The instantaneous internal HDs were taken as the maxima of these probabilistic maps. These estimates faithfully tracked the head orientation of the mouse during the period preceding cue rotation. The degree of realignment of the HD system was calculated as the decoder error: angular difference between the real HD and the internal HD at each time bin. Since not all cue rotations resulted in HD realignment, we excluded all cue rotation epochs that (1) resulted in less than 45 degrees of mean decoder error in the following 200 s epoch, and (2) occurred when the animal was stationary in the preceding epoch (average velocity < 2 cm / sec).

We have observed that in our paradigm the realignment was not instantaneous but often lasted for several seconds, independently of the degree of Gaussian smoothing applied to the spike trains. In order to estimate the rate at which the HD system remaps, we fitted a sigmoid curve to the decoder error values following each cue rotation using the *sigm_fit* function (https://www.mathworks.com/matlabcentral/fileexchange/42641-sigm_fit). We defined the beginning and end of realignment epochs as the timestamps corresponding to the values of 0.01 and 0.99 of the normalized sigmoids. We then, for each cell, calculated a HD tuning curve for the remainder of each cue epoch (from the end of realignment to next cue rotation), and computed the cross-correlation (see above) between HD tuning curves from consecutive epochs. For each cell, the degree of realignment was defined as the tuning curve offset which results in highest correlation coefficient. The difference in realignment between FS and HD cells was defined as, for each FS cell, the angular difference between its degree of realignment and the average realignment of HD cells in the same epoch.

Classification of sleep states

Sleep scoring was performed using the automated SleepScoreMaster algorithm [67,68] (Buzsaki laboratory, https://github.com/buzsakilab/buzcode/tree/master/detectors/detectStates/SleepScoreMaster). Briefly, the wide-band signal was downsampled to 1.25 kHz and used as the LFP signal. Electromyograph (EMG) was computed from correlated high-frequency noise across several channels of the linear probe.

Pairwise spike rate coupling

Quantification of pairwise spike rate coupling between cells was quantified using a General Linear Model (GLM) according to the method described in [51]. Spike trains were binned in 100 ms bins and smoothened in 100 ms s.d. Gaussian windows. The population firing rate was calculated by aggregating all spike times from all recorded units in a given recording and processing them in the same manner as single spike trains. Both binned trains were then restricted to either WAKE or REM epoch (see above).

The GLM was fitted using the MATLAB 'glmfit' function. The binned spike train of cell A was modelled as a Poisson process, as a function of both the binned spike train of cell B and the binned population firing rate, using a log link function. The model produced a coefficient of coupling between the spike trains of cells A and B ('Beta'), as well as a coefficient for the coupling of cell A to the population firing rate ('Beta-pop'). The procedure was repeated by offseting the spike train of cell A by ± 10 seconds in 100 ms intervals, to yield the equivalent of spike train cross-correlogram that discounts the coupling of cell A to the local population rate. Since this procedure, unlike Pearson's correlation, is not symmetric, it was repeated by substituting cell A and cell B and averaging the coupling coefficient values at equivalent offset intervals. A cell pair was removed from the analysis in rare cases when the 'glmfit' function identified the model as ill-fitted or reached the iteration limit.

Visualization and analysis of the ring manifold

For visualizing the HD manifold during WAKE, HD cell spike times from the whole epoch were binned into population vectors in 200 ms bins, smoothened in 400 ms s.d. Gaussian windows and a square root of each value was taken. Then, non-linear dimensionality reduction was performed using the Isometric Feature Mapping (Isomap) algorithm [43] implemented in the Matlab Toolbox for Dimensionality Reduction (https://lvdmaaten.github.io/drtoolbox/). The parameters were set to 12 nearest neighbours and 3 dimensions – the latter to inspect if there is no higher dimensional manifold in the data. Shuffled Isomap embeddings were computed by shifting each cell's binned spike train in time by a random number of bins.

Internal HD at each time bin was then calculated as a four-quadrant arctangent of the two Isomap dimensions (range: -180° to 180°). Importantly, the internal HD generated this way has arbitrary directionality (clockwise/anticlockwise) and an arbitrary point of origin. To calibrate it, Isomap directionality was established by computing the Isomap error as the difference between real HD values and (1) internal HD values and (2) internal HD multiplied by -1, and selecting the directionality with error of smaller circular variance. Internal HD tuning curves were then computed as the ratio between histograms of spike count and total time spent in each internal HD in bins of 1 degree and smoothed with a Gaussian kernel of 3° s.d. Real HD tuning curves were computed by downsampling the real HD into 200ms bins and applying the same procedure as above. In order to correct for the arbitrary point of origin, HD tuning curve cross-correlations (see above) were computed between each real and internal HD tuning curve of each HD cell, and the mean offset of maximum correlation was then used to circularly shift all tuning curve vectors by

the equivalent number of bins. While this procedure (as well as Isomap mapping in general) was dependent on the real HD tuning of HD cells, it was independent of FS cell tuning. Control HD tuning curves were computed by time-reversing the Isomap angle (see above).

For the comparison between internal HD tuning curves during WAKE and REM, population vectors across WAKE and REM were computed in the same manner as above. WAKE population vectors were then randomly downsampled to equal in number to the REM population vectors. Isomap algorithm was then run on both WAKE and REM population vectors together. Internal HD was computed in the same way as above. HD tuning curves were computed in bins of 6 degrees and smoothed with a Gaussian kernel of 1° s.d for both real and internal HD. Larger bin size was chosen due to sometimes uneven sampling of virtual HDs during REM.

Fourier analysis of HD tuning curves

To decompose tuning curves into Fourier series, we projected the tuning curves onto a basis of sine and cosine functions whose frequencies were the harmonic of the unit circle, i.e. from the fundamental frequency (period of 360°) to the highest possible frequency (2°, the inverse of the Nyquist frequency as tuning curves are computed in 1° bins). The power, or Fourier coefficients, at a particular frequency was defined as the root mean square of the projection values onto the sine and cosine basis at that frequency. Similarly, the phase was defined as the arctangent of the projections. The validity of the projection was verified by checking that the sum of squared Fourier coefficients is equal to the variance of the tuning curves (Parseval's identity), which was indeed the case (**Figure S2E**). Since higher Fourier components likely represent noise fluctuations in the tuning curves, we focused our analysis on the relative power of the first ten Fourier components, normalizing their individual power values to the sum of their power.

Kullback–Leibler (KL) divergence was used as a measure to assess the similarity between the individual Fourier spectra and the population means. While KL divergence is regularly used to compare probability distributions, we deemed it appropriate to apply it to normalized Fourier spectra as they were mathematically indistinguishable from probability distributions.

Isomap analysis of HD tuning curve auto-correlograms

Cross-validated autocorrelograms of each cell's tuning curve were computed as described above. Then, non-linear dimensionality reduction was performed using the Isometric Feature Mapping (Isomap) algorithm [43]. The parameters were set to 12 nearest neighbours and 2 dimensions. When mapping the first three Fourier components onto the resulting embedding, we normalized their power to the total sum of their powers.

Anatomical tract tracing

VGAT-Cre mice were injected with an adeno-associated virus vector (AAV 2/9 CAG-Flex-EGFP, titer: 4-5 x 10^{12} GC/ml, Neurophotonics, 500 µl per injection site) bilaterally into the thalamic reticular nucleus as described above. Four weeks after injections, animals were perfused transcradially with 4% PFA in phosphate-buffered saline and their brains were then cut coronally in 40 µm sections with a freezing microtome. The sections were counterstained with blue NeuroTrace and mounted on sides with Coronal z-stacks of the sections containing the rostral thalamus were taken with a Leica SP-8 confocal microscope at x10 magnification, using the same settings for all sections. GFP signal was acquired using the 473 nm excitation laser line. Z-projections of each stack were then obtained using ImageJ software. Quantification of anterograde tracing was done in ImageJ. The images were converted to grayscale and rectangular regions of interest (ROI) were defined within each thalamic nucleus. Average pixel intensity per ROI was then calculated using the 'Measure' function.

Thalamic gain modulation analysis

Epochs of optogenetic stimulation (light ON) consisted of time periods when the laser was switched on (240 pulses of 2 sec duration, 240 sec per session). Control epochs (light OFF) were defined as time-periods in-between light pulses (240 periods of 4 sec duration, 960 sec per session). Light ON and light OFF tuning curves were computed from these periods. For analysis of tuning curve width, HD tuning curves were then computed in bins of 1 degree and smoothed with a Gaussian kernel of 3° s.d. For analysis of additive and multiplicative gain, in order to preserve the independence of individual angular bins, HD tuning curves were then computed in bins of 6 degrees with no Gaussian smoothing applied. Light ON and light OFF tuning curves for each cell were then normalized by dividing them by the maximum value of the light OFF tuning curve. To calculate the additive and multiplicative factors for each cell, a linear fit between light ON and light OFF tuning curve vectors was then obtained using the Matlab *polyfit* function. The slope of the resulting linear fit and its Y intercept were then taken as multiplicative and additive gain values, respectively.

Data analysis and statistics

All analyses were conducted using software custom-written in Matlab R2020b (Mathworks). Unless otherwise specified, statistical comparisons were performed with Mann-Whitney U test, Willcoxon Signed Rank Test or ANOVA with multiple comparisons, where applicable.

Data Availability

The datasets generated and/or analyzed in this study will be made available online at time of publication.

Code Availability

Code will be available upon request.

Acknowledgment

This work was supported by a Canadian Research Chair in Systems Neuroscience, CIHR Project Grant 155957, NSERC Discovery Grant RGPIN-2018-04600, and the Canada-Israel Health Research Initiative, jointly funded by the Canadian Institutes of Health Research, the Israel Science Foundation, the International Development Research Centre, Canada and the Azrieli Foundation 108877-001 (AP); a Sir Henry Wellcome Fellowship (AD). The authors thank Blake Richards, Stuart Trenholm and members of the Peyrache Lab for their comments on an earlier version of this manuscript.

Author Contributions

A.D. collected the data with the help of S.S.C., E.B., and G.R.V.; A.D. and A.P. analyzed the data with the help of P.O. and E.K.; A.D. and A.P. wrote the manuscript with inputs from E.R.W.; A.P. supervised the project.

Competing Interests

No competing interests disclosed

Materials & Correspondence

All correspondence should be directed to Adrien Peyrache at adrien.peyrache@mcgill.ca